FABRICATION OF SITE-CONTROLLED QUANTUM STRUCTURES FOR OPTOELECTRONIC DEVICES

BY

CHIEN-CHIA CHENG

DISSERTATION

Submitted in partial fulfillment of the requirements
for the degree of Doctor of Philosophy in Electrical and Computer Engineering
in the Graduate College of the
University of Illinois at Urbana-Champaign, 2012

Urbana, Illinois

Doctoral Committee:

Adjunct Professor Keh-Yung Cheng, Chair
Adjunct Professor Kuang-Chien Hsieh
Professor Milton Feng
Professor Jianming Jin

ABSTRACT

Over the past two decades, there has been great interest in integrating semiconductor quantum dots (QDs) into electronic and optoelectronic devices, utilizing the three-dimensional quantum confinement effect to improve device performance as well as to create devices with new functionalities. However, despite its prevalence in fabrication of QDs, self-assembled QD growth via the Stranski–Krastanov growth mode does not provide much control over QD size, spatial position, and uniformity, and thus can only be used in limited applications. Contrarily, site-controlled QD (SCQD) fabrication has been considered a promising alternative for its abilities to improve QD homogeneity and precisely address the positions of QDs.

In this study, two pathways to fabricate SCQDs are developed and explored by utilizing soft photocurable nanoimprint lithography (soft NIL) to create nanoscale patterns. The first is a bottom-up method which leads to the formation of "regrown QDs". In this approach, high optical quality InAs QDs are regrown in designed nucleation sites over GaAs substrate, and the effects of process and growth parameters on the structural and optical properties of regrown QDs will be examined. In contrast, "pillar QDs" are fabricated from quantum wells (QWs) by the top-down approach, in which strained InGaAs single QW patterned by soft NIL is etched into pillar QB array. Extremely narrow photoluminescence linewidth from a pillar QB array suggests an unexplored phenomenon due to interaction between periodically-arranged optical emitters. A new model, quantum structure lattice, to explain the experimental results will be proposed and discussed.

To my family

ACKNOWLEDGMENTS

First of all, I would like to express my sincere gratitude to my advisor, Professor Keh-Yung Norman Cheng, for his continuous guidance and support through my graduate life. It is indeed a privilege to work in his research group for so many years. I have been greatly influenced and inspired by his expertise and professionalism in the field of MBE, and attitude and philosophy toward scientific research. I would like to acknowledge Professor Kuang-Chen Hsieh for fruitful discussions and his kindness to financially support my work in the past year. I would like to thank Professor Milton Feng for extending the support of his group members to complete my research and his enthusiastic assistance in many aspects. I would also like to thank Professor Jianming Jin for his constructive discussion and suggestion about this study.

Needless to say, this work couldn't be done without the support of former group members. I would like to thank Dr. Bing-Ruey Barry Wu for introducing me to the MBE group. I want to thank Dr. Chiun-Lung Tsai for her time and patience in training me on the operation of the MBE system. And, I appreciate the collaborative efforts from Dr. Kevin J. Meneou. I am also thankful for Dr. Chi-Chih Keith Liao for his help on vacuum system maintenance and productive discussions.

Most importantly, I am indebted to my father, Ta-Liang, my mother, Mei-Jung, my brother, Orpheus, and sister, Sandra, for their constant love and continuous support throughout the years. I am also graceful for my wife, Jessie, for her endless encouragement and devotion.

This work has been supported in part by the U.S. Army Research Office (Dr. W. Clark and Dr. M. Gerhold W911NF–09–1–0490) and DARPA (HR0001–04–1–0034) in the early stage of the program. Patterning was carried out in part in the Frederick Seitz Materials Research Laboratory Central Facilities, University of Illinois, which are partially supported by the U.S. Department of Energy under Grant Nos. DE-FG02-07ER46453 and DE-FG02-07ER46471.

TABLE OF CONTENTS

CHAPTER 1 INTRODUCTION

Over the last two decades, there has been great interest in integrating semiconductor quantum dots (QDs) into electronic and optoelectronic devices, utilizing the three-dimensional (3-D) quantum confinement effect to improve device performance as well as create devices with new functionalities [1-3]. By definition, a QD is a nanoscale structure smaller than 100 nm in all three dimensions. Due to the introduction of quantization effects, this tiny structure is endowed with the ability to control the electron/hole density of states and the number of confined electrons / holes inside it by adjustment of QD dimension. Incorporation of QD in the device structure is demonstrated to enhance electrical and optical performance of the device. For instance, when QDs are used as the active medium of a semiconductor laser, strong confinement of electron and hole wave functions in QDs results in ultrahigh material and differential gains, reduction of threshold current density, and, most importantly, improved temperature stability of threshold current [4]. Moreover, some theoretically superior performances are also anticipated for QD lasers over quantum well (QW) counterparts, including lower chirp and higher modulation bandwidth [5].

For the time being, fabrication of semiconductor QDs is mostly done by epitaxial growth in ultra high vacuum environment. Generally speaking, there are three modes of homoepitaxial/heteroepitaxial growth in semiconductor: Frank-van der Merwe (FvdM) growth, Volmer-Weber (VW) growth, and Stranski-Krastanow (SK) growth, representing layer-by-layer growth, island growth, and layer-by-layer plus island growth, respectively. During growth of lattice-matched material, two-dimensional FvdM growth generally

dominates, resulting in atomically smooth growth surface. However, in the growth of lattice-mismatched materials, initial growth starts with FvdM mode. With increase of layer thickness, strain between different materials begins to accumulate. Once the thickness exceeds a critical thickness, which highly depends on the chemical and physical properties of the substrate and film, SK growth mode will take place instead by forming isolated islands to relax the overall energy. The islands formed by SK grow mode are referred to as self-assembled quantum dots (SAQDs) owing to the nature of lattice-mismatched heteroepitaxial growth.

Thus far, SAQDs growth based on SK growth mode is the most prevalent way to realize high quality QDs. Major advantages of SAQDs include simple growth techniques and superb optical qualities [6]. During epitaxial growth of SAQDs, the change of growth mode from FvdM to SK can be directly observed through transition of the reflection high-energy electron diffraction (RHEED) patterns. As RHEED patterns change from streaky to spotty, a layer-by-layer growth mode is replaced by a corrugated three-dimensional island. Controlling the density, size, and uniformity of SAQDs can be realized through optimization of growth conditions, such as V/III ratio, growth temperature, growth rate, or growth interruption time.

This approach provides not only *in situ* growth for fabrication of QDs with high density and optical quality, but avoids potential damage and contamination arising from *ex situ* process techniques. Various compound semiconductor QDs adopting SK growth method have been extensively studied, including In(Ga)As / GaAs, InAs / InP, and In(Ga)N / GaN. Moreover, QD-based lasers, detectors and other optical devices have been successfully demonstrated [7, 8].

Although it is relatively easy to generate defect-free nanostructures, SAQDs are still not the best choice to achieve superb performance owing to several inherent drawbacks. To begin with, QD size distribution is sensitive to growth conditions, and often leads to a broader photoluminescence (PL) linewidth. Then, dimensions of SAQDs could only be tuned by changing growth conditions or material composition, and the optimization is usually time-consuming. Lastly, due to the statistical nature of the self-assembling process, random nucleation sites of SAQDs make this approach difficult to precisely address an individual QD in certain applications, such as single photon emitters. In short, SAQD growth via the SK growth mode does not provide much control over QD size, uniformity, and spatial position, which is essential for device applications. Consequently, improving homogeneity while precisely manipulating the position of the QDs becomes an important issue, which leads to the concept of site-controlled quantum dots (SCQDs) [9-11].

To achieve superior performance to SAQDs, various strategies are proposed to climb up the hierarchy of QDs, not only in size and shape, but also in lateral alignment. The idea is to pattern the substrate with designed features, usually nanopores, prior to epitaxial growth, and then allow materials to assemble at the desired locations, forming SCQDs. Take InAs/GaAs QDs as an example: the core concept of growth is to use high growth temperature and low growth rate such that In atoms will migrate on the surface until getting caught in nanopores while they are re-evaporated in flat regions with fewer atomic steps. Since the late 1990s, SCQDs have been realized through the growth on patterned substrates prepared by electron beam lithography (EBL) [10,12], focused ion beam (FIB) [13], and a combination of atomic force microscope tip-induced oxidation,

atomic hydrogen etching/cleaning, and droplet epitaxy [14]. Self-organized material, such as nano-channel alumina, is also used to define the nucleation sites for high density SCQDs [15].

Although improved QDs size distribution and narrowed PL linewidth at very low temperatures have been accomplished [11], devices with improved optical performance have not been demonstrated. Surface damage caused by high-energy beams used in these patterning techniques is generally accepted as the culprit for the poor optical quality. Damage around QD nucleation sites acts as a nonradiative recombination center, degrading optical quality of subsequently grown QDs. Furthermore, due to the serial nature of EBL and FIB lithography, the cost would be extensive if a large number of devices need to be fabricated. As a result, it is necessary to develop alternative approaches for the fabrication of high quality SCQDs cost efficiently. In the meantime, there are other constraints for a technology to be considered and adopted for future SCQD manufacturing. Firstly, the technology must be fully compatible with existing III-V compound semiconductor process, and crystal growth techniques for easy integration. Secondly, the technology has to be easily applicable for mass production. And, most importantly, functioning as the light emitters, the produced SCQDs have to exhibit high luminescence efficiency, which is undoubtedly crucial for optoelectronic applications.

Taking every factor into account, one potential candidate to fulfill most of the requirements is nanoimprint lithography (NIL). First proposed as a technique for general sub-micron patterning in the mid-1990s, NIL is promising for high-throughput and low-cost nanostructure fabrication through parallel patterning, and has been shown to fabricate nanoscale devices with high reproducibility. Features with diameter less than 10

nm are also demonstrated [16, 17]. Recently, soft photocurable nanoimprint lithography (soft NIL), branched from NIL, is proposed to create patterns for fabrication of compound semiconductor nanostructures [18]. In addition to meeting most of the requirements mentioned above, most importantly, soft NIL pattern transfer process is achieved by deforming the photoresist through physical contacting, and no high-energy beam is involved, thus avoiding potential damage to the substrate. Based on these facts, soft NIL is exclusively used in this study to pattern semiconductor substrates, and more process will be detailed in the beginning of Chapter 2.

In this dissertation, two approaches utilizing soft NIL are explored to form site-controlled quantum structures. The quantum structures fabricated by these two approaches are named “regrown QDs” and “pillar QDs”. Solid source molecular beam epitaxy (SSMBE) is exclusively used for all the epitaxial growth. Figure 1.1 and Figure 1.2 show the process flow for the fabrication of regrown QDs and pillar QDs, respectively. A brief explanation of how these two approaches work is described as follows. First, a piece of semiconductor is prepared by epitaxially growing desired structures on top of a substrate. Then, soft NIL is used to create an array of designed patterns on the surface of semiconductor. The patterns are transferred into the substrate via either wet etching or dry etching. In the last step, the semiconductor is loaded into the molecular beam epitaxy (MBE) chamber for subsequent regrowth. The following sections will describe the process in more detail.

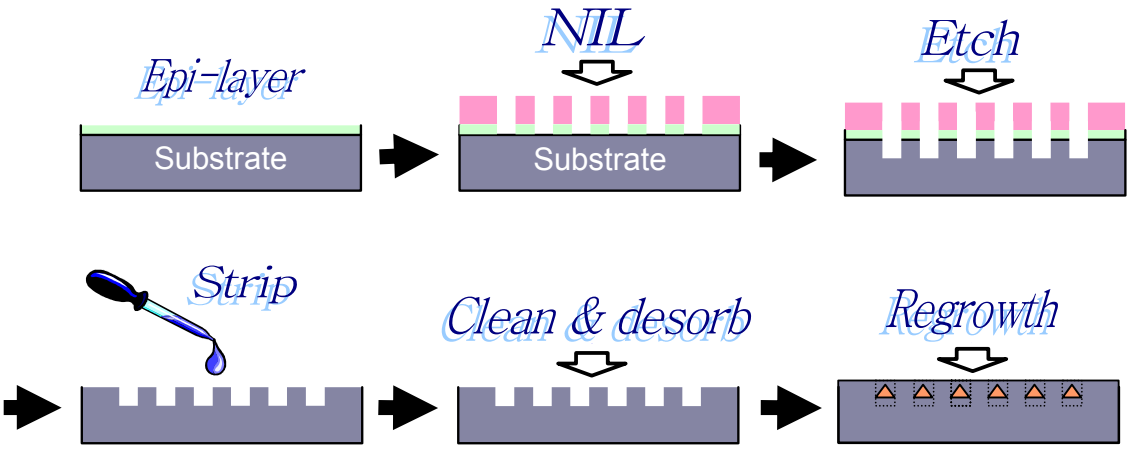

Figure 1.1 Process flows of soft nanoimprint lithography and epitaxial regrowth for the fabrication of regrown QDs. A semiconductor substrate is coated with silicon nitride in the first step, followed by a layer of photoresist. Soft nanoimprint lithography is performed to transfer patterns into semiconductor substrates by either wet etching or dry etching. After removal of the nitride layer, QDs are regrown in the designed nanopores and covered with a cap layer.

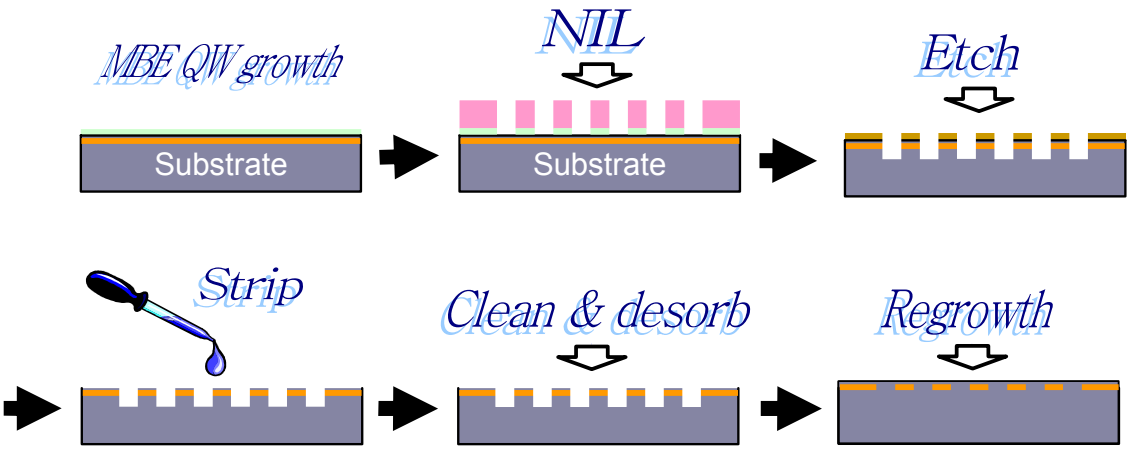

Figure 1.2 Process flows of soft nanoimprint lithography and epitaxial regrowth for the fabrication of pillar QDs. A shallow quantum well is first grown on a semiconductor substrate. Soft nanoimprint lithography is used to produce a patterned photoresist layer atop a silicon nitride layer. By wet etching or dry etching through the quantum well and stripping the etch masks, MBE overgrowth of the cap layer completes the pillar QDs.

In Chapter 2, the fabrication process of soft NIL is explained in detail, and the impacts of different process parameters on the morphology of nanopores are investigated. The effects of growth parameters, such as buffer layer thickness and arsenic overpressure, on the luminescent properties of regrown QDs are also discussed. In Chapter 3, process development of pillar QDs is presented. A new model, quantum structure lattice model, is proposed to explain peak emission energy shifts in photoluminescence measurement of pillar QDs. Further experimental results support this model plausibly. In the end, the summary and future work will be described in Chapter 4.

All the characterization tools used in this work are listed below. Scanning electron microscope (SEM) images are taken using a Hitachi S-4800, and a Digital Instruments 3100 atomic force microscope (AFM) with tapping mode is used to measure the surface morphology. Photoluminescence (PL) spectra are measured at room temperature and 77 K in a liquid-nitrogen cooled cryostat. A frequency-doubled Nd:YAG laser source with a wavelength of 532 nm is used to excite the samples, and the excitation power density is 20 W/cm^2. The signal is collimated by lenses into a 0.5 m spectrometer with a lock-in amplifier and detected by a liquid-nitrogen cooled Ge photodetector.

CHAPTER 2 PROCESS DEVELOPMENT OF REGROWN QUANTUM DOTS AND CHARACTERIZATION RESULTS

2.1 Patterning Process

Nanoimprint lithography [19] is a high-throughput and high-resolution patterning technique. The concept of NIL is to replicate a surface pattern from a mold into resists by mechanical contact and detachment. During the process, resists are squeezed by pressure and capillary forces to conform to the surface of pattern, and hardened by thermal treatment or ultraviolet (UV) light exposure. Separating the mold and the resists completes the NIL process. Application of NIL in semiconductor material and electronics has been extensively investigated since the 1990s and sub-10-nm nanostructure is also demonstrated [17].

Among various branches of NIL techniques, the most widely used is ultra-violet NIL (UV-NIL) [20]. In this technique, a layer of ultra-violet sensitive polymer is coated on semiconductor substrates. The polymer is similar to what has been used in photolithography, but has much lower viscosity for rapid dispensing and filling of mold cavities. After the UV-transparent mold and the semiconductor are brought into intimate contact, the polymer layer is exposed under UV light. Cross-linking and photopolymer conversion hardens the polymer and makes the separation more easily. Nonetheless, the main disadvantage is constraints on the morphology of the mold and sample. The step of contacting the mold to the substrate is often critical, and requires further attention. This disadvantage promotes the use of soft lithography, in which adequate contacting could be achieved by placing a soft and flexible polymeric mold atop semiconductor by hand.

Soft NIL is a term coined to describe the technique for patterning semiconductor substrates that was developed previously [21]. The term attempts to capture the marriage of soft lithography, i.e. the use of a flexible PDMS mold, with an application and process design more closely resembling work on UV-NIL. In essence, the technique used here is similar to what is described in much of the literature on UV-NIL, but with a soft mold instead, hence the name "soft lithography." Soft NIL is used in these experiments to transfer a two-dimensional (2-D) pattern to the photoresist atop semiconductor substrates. Advantages of this soft lithography technique are rock bottom costs for materials and tools and high throughput, combined with the ability to accurately reproduce features smaller than 100 nm. These qualities make soft NIL a perfect fit for this application, and many others in optoelectronics. The main disadvantages would be limitations on multilayer alignment, and problems with replicating patterns that combine large (>1000 nm) features with small features. Nonetheless, the disadvantages are no limitation at all in pursuing QD lasers using the approach in this dissertation.

2.1.1 Soft Nanoimprint Lithography

The pattern used for the fabrication of regrown QDs is a 2-D array of square pores with 100 nm on a side and 200 nm in periodicity as diagrammed in Figure 2.1. The depth of the pores is designed to be 70 nm. The original pattern to be replicated is fabricated on a silicon (Si) template using interference lithography. The template is one quarter of a 4 inch wafer of silicon with an anti-stick layer on the patterned side, and was purchased from Nanonex Corporation, Monmouth Junction, NJ, USA.

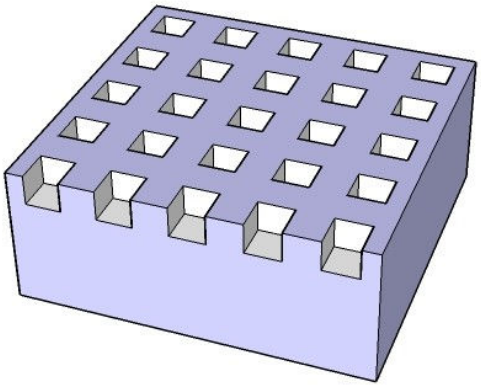

Figure 2.1 Schematic diagram of the silicon template used for the fabrication of regrown QDs. The pattern is a 2-D array of square pore. The pore is 100 nm on a side with a periodicity of 200 nm, and the depth is 70 nm.

Figure 2.2 shows the process flow of the soft NIL by which the pattern of the template is replicated in a layer of PR on a planar sample. The sequence of the steps involved is detailed below. The first step is to coat the Si template with polydimethylsiloxane (PDMS) which forms the mold. The mold consists of two major parts. A bottom layer of "hard PDMS" is spin-coated first and then a layer of "soft PDMS" is poured on top, following the work published previously [18]. The hard PDMS will hold the pattern information while the soft PDMS acts as a handle and protects the hard PDMS from cracking. Then the PDMS / master are placed in an oven at 100 °C for 24 hours in order to fully cure the PDMS. Then, the PDMS mold is cut and peeled away from the template, and is ready to be used for imprinting.

To prepare a substrate, such as GaAs or InP, for soft NIL, a 50-nm layer of silicon nitride or silicon dioxide needs to be deposited on the substrate using plasma-enhanced chemical vapor deposition (PECVD) before processing. This layer acts as a sacrificial layer in order to facilitate removal of the imprint PR layer after patter transfer. The PR used in this study cannot be removed by any known wet chemical that will not also react

with the GaAs or InP substrate. The deposition of this layer is essential for preventing any PR residue remaining on top of the semiconductor. Either hydrofluoric acid or buffered oxide-etch solution can be used to completely etch away this sacrificial layer while etching of GaAs or InP is negligible. In the first part of the imprinting step, the sample is cleaned with acetone and isopropyl alcohol (IPA), and blown dry with dry N_2. Then it is loaded into a spin coater. A small amount of PR is dispensed onto the sample and the spin coater is immediately energized with settings of speed 4000 rpm/s. The mold is then lowered until it is resting on the sample.

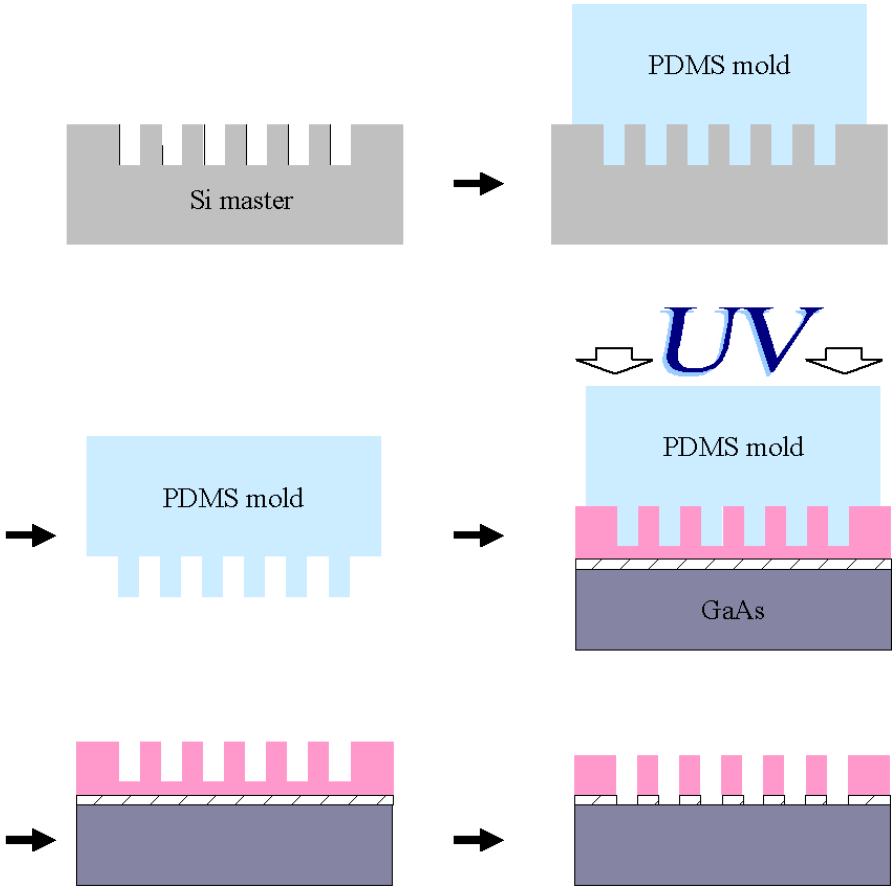

Figure 2.2 Process flow of soft NIL. First, the pattern on the master is replicated on a PDMS mold, by pouring liquid PDMS on the master, thermally curing the PDMS, and peeling away the mold. Then the PR is coated on the substrate, and the mold brought into contact with the PR. Finally, cured by UV light, the residual PR layer and underlying nitride layer are etched through by reactive ion etching (RIE).

To achieve intimate contact, the tweezers are used to press the mold onto the substrate with moderate pressure. The idea is only to get all areas of the mold to touch the photoresist. Once the mold touches the photoresist, capillary action sucks the photoresist into the mold in that area and all voids of the mold are filled. Next, the sample and mold are carefully loaded together into a contact aligner or other exposure tool and exposed at a UV dose of approximately 18 J. The PDMS is then peeled from the sample to complete the imprinting step. After the mold is cleaned with acetone and IPA and blown dry with dry N_2, the PDMS mold is ready to be used again. It may be used dozens of times before it needs to be replaced.

At this point the pattern is fixed into the PR layer, but a "residual layer" of PR remains on the substrate at the locations of the nanopores. To facilitate pattern transfer, a standard process is required to remove this residual layer while leaving the rest of the PR layer intact. A short RIE step designed to etch photoresist in an anisotropic fashion is used to remove the residual layer. For simplicity, in the same RIE step, an etching process is added to remove the silicon nitride layer at the locations of the nanopores. This RIE step is termed the breakthrough etch. The standard process is 40 s RIE using oxygen gas, followed by 120 s RIE using CHF_3. In both RIE processes, the pressure is set to 10 mTorr, the gas flow to 10 sccm and the radio-frequency (RF) power to 150 W. Experiments confirm the bulk of the photoresist is virtually unaffected while the residual layer and underlying silicon nitride is completely removed by this process.

2.1.2 Pattern Transfer Etching and Pre-Growth Surface Treatment

The substrate used in this work is (100) semi-insulating GaAs wafer, and all samples are several cm^2 in size, limited by the size of silicon NIL master. The GaAs substrate is first coated with 50 nm silicon dioxide followed by a UV-curable PR of ~120 nm thick. Next, the soft NIL technique is used to replicate the designed pattern in the silicon dioxide and PR layers. The pattern used in this study is a large area square array of 100 nm by 100 nm square pores on a 200 nm pitch, yielding an array density of 2.5×10^9 cm^{-2}. After being subjected to the entire soft NIL process, the GaAs samples can be treated by either wet etching or dry etching to finish pattern transfer.

A solution of ammonium, hydrogen peroxide, and deionized water mixture is used for wet etching. The mixture of the solution is 1:1:790 $NH_4OH:H_2O_2:H_2O$ with a nominal etching rate of 18 nm/min. The wet etching step is especially important for

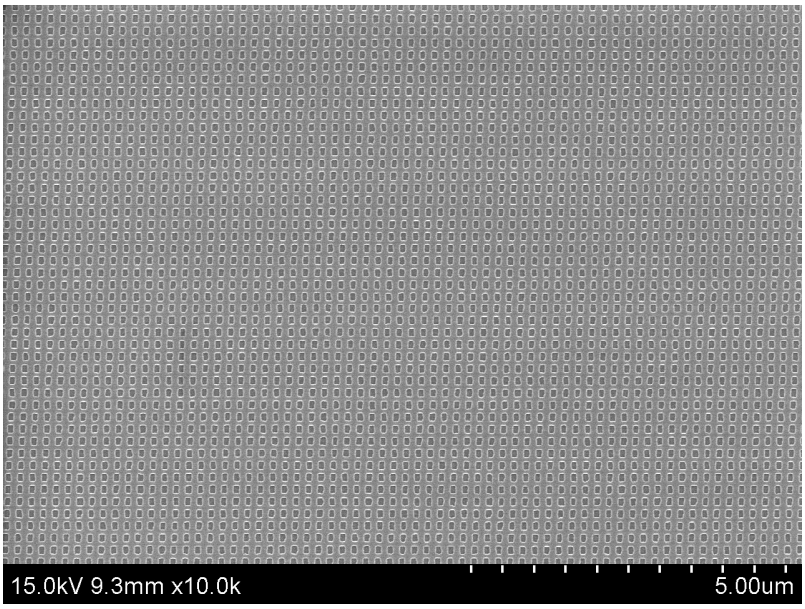

Figure 2.3 Scanning electron micrograph (12 μm × 9 μm) of a cm^2 size GaAs substrate patterned with 100 nm × 100 nm nanopores and a periodicity of 200 nm.

removing residual ion-related damages within nanopores. The dry etching is carried out in an inductively coupled plasma RIE (ICP-RIE) system using silicon tetrachloride at 40 W RF power and 100 W ICP power. A detailed comparison of wet etching and dry etching technique will be described in the following section.

Figure 2.3 shows the SEM image of the nanopore array patterned on a GaAs substrate using wet etching. Patterns are transferred in parallel fashion from the silicon master into GaAs with high fidelity. In addition, very low defect density such as missing nanopores is observed over a large area scanned.

AFM surface images shown in Figure 2.4(a) and 2.4(b) illustrate the variation of surface morphology by wet etching and dry etching techniques prior to QD growth, respectively. AFM line scans of wet- and dry-etched samples are shown in Figure 2.4(c) and 2.4(d), and the etching depths are 15 nm and 25 nm, respectively. Patterns prepared by wet etching maintain the original square shape with smooth edges while irregularity over edges of nanopore is seen in dry-etched sample. The imperfect transfer observed in dry-etched samples is ascribed to a non-optimized residual layer etching in the current imprint process, and could be improved. The effect of etching methods on the properties of subsequently grown SCQDs will be discussed in the following section.

In order to achieve high QD quality, a set sequence of cleaning steps is carried out on all patterned samples before MBE growth. To begin with, samples are treated by oxygen plasma, followed by ultrasonic cleaning in acetone, methanol, and isopropanol. Then, a sequence of hydrochloric acid and sulfuric acid etching is applied, intended to remove surface oxides and passivate the surface, respectively. Finally, surface treatment procedure ends with a thorough deionized water rinse and nitrogen blow dry. Afterward,

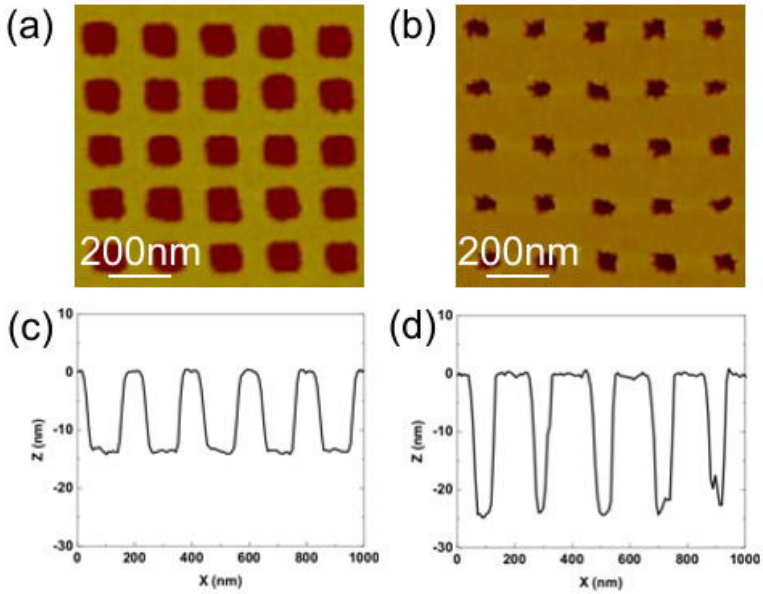

Figure 2.4 AFM images (1 μm × 1 μm) and line scans of patterned GaAs substrate using: [(a) and (c)] wet etching and [(b) and (d)] dry etching techniques prior to QDs regrowth.

samples are mounted on a molybdenum puck with high purity indium, and loaded in a solid-source MBE system equipped with a valved arsenic effusion cell.

2.2 The Solid-Source Molecular Beam Epitaxy System

All the structures studied in this work are grown using a Superior Vacuum Technology Associates (SVTA) MBE system. The system consists of an ultra high vacuum growth, transfer, and load-lock chamber. A sample transfer and load-lock mechanism is applied to introduce samples into the system and transfer them between chambers. A CTI-Cryogenics CT-100 cryopump is used to pump the loading lock to a baseline pressure of 3×10^{-8} torr. The transfer chamber is equipped with a Perkin-Elmer ion pump which pumps the chamber to a baseline pressure of 5×10^{-10} torr. The substrate is mounted on a molybdenum (Mo) block using high-purity indium metal to form a good

thermal contact. A bake-out heater installed in the transfer chamber bakes each sample at 250 °C for 5 min to remove residual water on the wafer or Mo puck before it is transferred into the growth chamber.

The growth chamber is pumped by a combination of a CTI Cryogenics CT-8 cryopump and a Varian ion pump. Liquid-nitrogen-cool shrouds are used to reduce water-vapor partial pressure. A base pressure of $\sim 2 \times 10^{-9}$ torr in the growth chamber can be achieved with all effusion cells at their idle temperatures of 300 °C. The growth chamber background pressure is usually 2×10^{-8} torr when the effusion cells are at their respective growth temperature with all shutters closed. The monomer group-III fluxes (Ga, In, and Al) are produced using thermal evaporation effusion cells contained a pyrolytic boron nitride crucible in each cell. Solid arsenic is used as the group-V source material. An EPI 500V-As-4 arsenic valved cracker cell with a low-temperature sublimating crucible and a high-temperature cracking furnace is used to accurately control the supply of arsenic. Two dopant cells, silicon and beryllium, are used in the system to provide electron and hole doping, respectively. The growth chamber also carries an Oxford Scientific TC-50 thermal atomic hydrogen cracker that utilizes electron bombardment heating of a tungsten capillary to thermally dissociate the hydrogen gas passing through it. The produced atomic hydrogen removes oxygen and carbon by reduction to volatile hydrides and serves as surfactant promoting 2-D growth.

Growth rates are calibrated using RHEED intensity oscillations. RHEED patterns also provide information on crystal perfection, surface flatness, and surface reconstruction when a growth proceeds. The growth temperature is typically monitored by a substrate heater thermocouple and an infrared optical pyrometer. Due to block-to-

block and sample-to-sample variations, the substrate temperature is determined relative to the surface oxide desorption temperature of GaAs substrate. Substrate rotation at 6 ~ 7 rpm is always used to maximize growth uniformity.

2.3 Growth Optimization of Regrown QDs

After soft NIL pattern transfer and *ex situ* cleaning steps, the GaAs samples are loaded into the MBE system for QD growth. Prior to the epitaxial regrowth, desorption of native oxides on the sample surface is necessary. During the regrowth, InAs is deposited with a growth rate of 0.014 ML/s at 500 °C. After the deposition of InAs QD layer, a 120 s growth interruption under a constant arsenic flux is inserted to enhance the formation of QDs. After the regrowth, the sample is cooled to room temperature for surface morphology characterization and PL measurements.

2.3.1 Atomic Hydrogen-Assisted Desorption

As the dimension of patterns shrinks down to nanoscale, extra care must be taken during the *in situ* surface clean process to retain pattern integrity. It has been shown that the conventional thermal desorption used to eliminate surface oxides and contaminants can severely distort the nanoscale patterns even if the duration of high temperature treatment is short [22]. Therefore, a low temperature desorption process needs to be adopted in this study. As suggested by Petit *et al.*, filament-cracked atomic hydrogen is capable of removing surface oxide from GaAs substrate at very low temperature [23]. Additionally, atomic hydrogen-assisted desorption is demonstrated to be drastically reduce the carbon contamination at the interface [24]. So, surface morphologies subjected to conventional desorption and atomic hydrogen-assisted desorption are compared. For

conventional thermal desorption, samples are heated at 580 °C for 10 min. As for atomic hydrogen-assisted desorption, samples are exposed to thermally cracked atomic hydrogen for an hour with the samples held at 480 °C. Figure 2.5 shows AFM surface images and line scans of patterned GaAs substrates subjected to each cleaning regimen. For nanopatterned sample surface after atomic hydrogen-assisted cleaning, AFM scans shown in Figure 2.5(a) and 2.5(c) are almost unchanged from the wet etching prepared sample as seen in Figure 2.5(a) and 2.5(c). This fact confirms the ability of preserving nanoscale patterns by the low temperature hydrogen-assisted desorption approach. The edges of nanopores become slightly blunt after atomic hydrogen-assisted cleaning, but it does not have a noticeable influence on SCQDs formation. In contrast, as displayed in Figure 2.5(b) and 2.5(d), the sample surface becomes rough with uneven pore depth after a short 10 min thermal desorption at 580 °C. Based on this result, atomic hydrogen-assisted desorption is used exclusively in the remainder of these experiments.

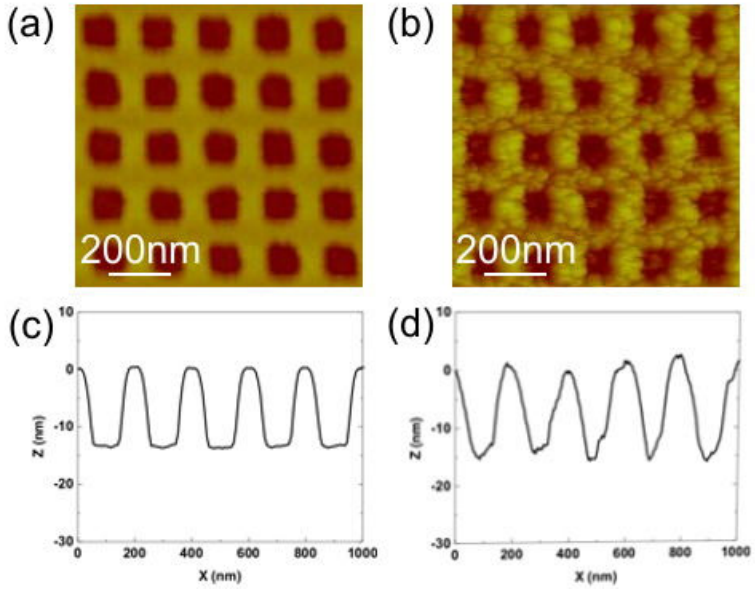

Figure 2.5 AFM images (1 μm × 1 μm) and line scans of patterned GaAs substrate: [(a) and (c)] after atomic hydrogen-assisted cleaning at 480 °C, and [(b) and (d)] after thermal desorption at 580 °C, prior to InAs QDs regrowth.

A series of experiments with different hydrogen pressure and cleaning time prior to InAs SCQD regrowth are conducted to optimize the surface cleaning procedure. During the desorption process, the surface reconstructions of GaAs are monitored by RHEED patterns. The desorption ends until a clear β(2×4) RHEED pattern is observed, which is a indication of a clean surface with minimal contaminants and defects [25]. Following the deposition of 30 ML GaAs buffer layer, a 3 ML InAs is grown and the room temperature PL measurement is carried out to compare the relative intensity among all SCQD samples. As shown in Figure 2.6, at a fixed desorption time of 50 min, the PL peak intensity increases by three times as the hydrogen pressure is increased from 2×10^{-7} torr to 2×10^{-6} torr. On the other hand, the PL intensity is enhanced by ten times when the cleaning time is doubled from 50 min to 100 min. According to the measured PL intensity enhancement, the atomic hydrogen cleaning process effectively removes not

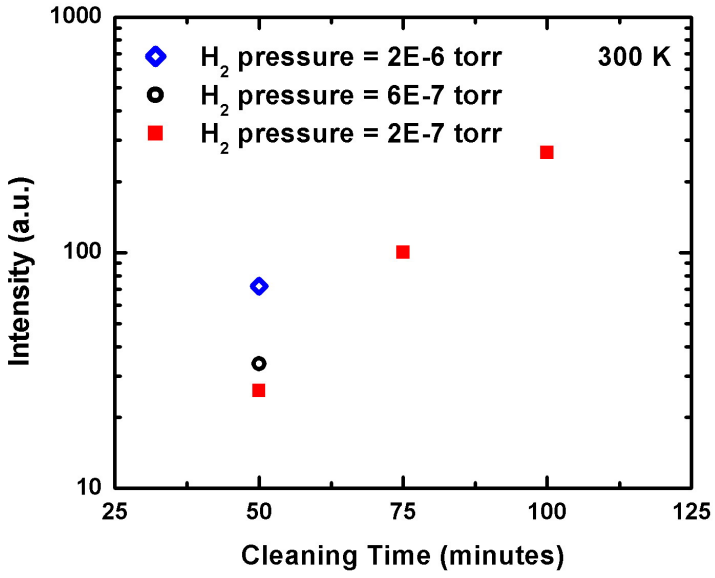

Figure 2.6 Room temperature PL intensity variation as functions of different hydrogen pressure and cleaning time. PL spectra are measured from SCQD samples after the deposition of 30 ML GaAs buffer layer and 3 ML InAs.

only surface oxides, but also contaminants, which act as recombination centers at the regrown interface.

2.3.2 Wet Etching vs. Dry Etching

After *in situ* oxide desorption, a 30 ML GaAs buffer layer followed by 3ML of InAs is deposited on both wet-etched and dry-etched samples simultaneously for comparison. Surface morphologies of regrown QDs on wet-etched and dry-etched samples are shown in Figure 2.7(a) and 2.7(b), respectively. On both samples, no QDs are formed on the flat surface between nanopores, suggesting the growth parameters for SCQDs formation are appropriate. Furthermore, as shown in Figure 2.7(a), one single dot inside each nanopore is demonstrated on the wet-etched sample, and the average diameter and height are 63 nm and 9 nm, respectively. In contrast, multiple dots are formed in each nanopore on the dry-etched sample grown under the same condition as shown in Figure 2.7(b). The phenomenon is caused by the large surface roughness (root mean square value ≈ 1 nm) inside the nanopore generated during the dry etching process. It is observed that the rough surface morphology persists even after the growth of a 30 ML GaAs buffer layer and the rough surface provides multiple nucleation sites for InAs QD growth within each nanopore. Consequently, disordered nonuniform QDs are formed within each nanopore as displayed in Figure 2.7(b). On the other hand, the smooth surface on the bottom of wet-etched nanopores is more favorable for In adatoms to migrate and coalesce into uniform single dots via the SK growth mode, which is clearly seen in Figure 2.7(a).

As expected, owing to energetic beam related damages, no light emission is detected from dry-etched samples prepared under the current conditions. Therefore, only PL spectra from wet-etched SCQD sample as well as an unpatterned SAQD reference sample are shown in Figure 2.8. The SAQD reference sample is prepared by mounting a piece of unpatterned epiready GaAs onto the MBE sample holder alongside the

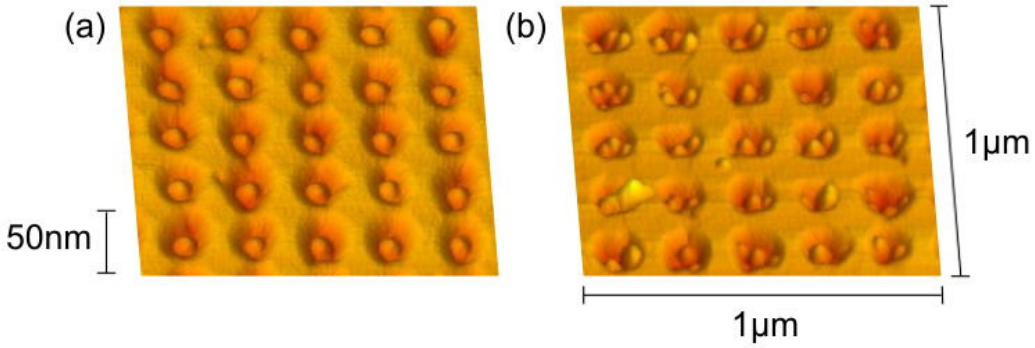

Figure 2.7 AFM images (1 μm × 1 μm) of patterned GaAs substrate after 30 ML GaAs buffer layer and 3 ML InAs layer are deposited on (a) wet-etched and (b) dry-etched GaAs patterned surfaces.

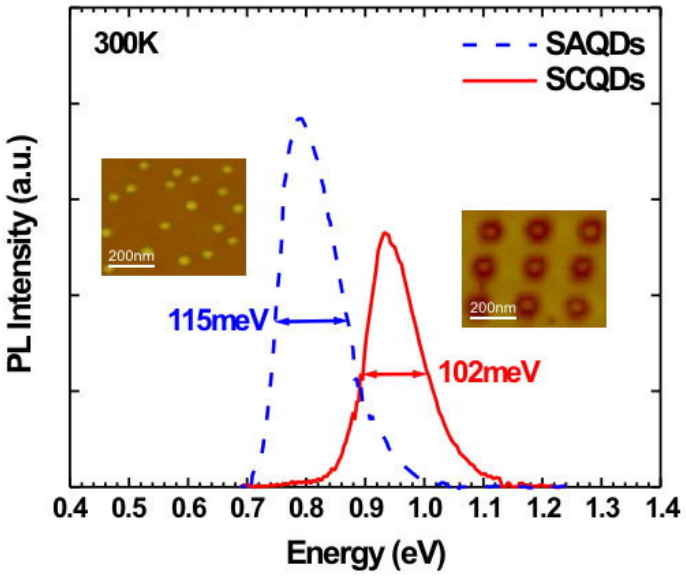

Figure 2.8 Room temperature photoluminescence spectra of self-assembled QDs (SAQDs) grown on unpatterned GaAs substrates (dashed line) and site-controlled QDs (SCQDs) grown on wet etching patterned GaAs substrates (solid line).

wet-etched SCQD sample. The two samples undergo oxide desorption and MBE regrowth together, resulting in SAQDs on the unpatterned piece of GaAs and SCQDs on the patterned piece. The PL peak position of the SCQD sample is 0.932 eV, compared to 0.792 eV for the SAQD case. The shorter peak wavelength for SCQDs originates from the fact that SCQDs has a wider base and a shorter height than SAQDs. The average height of SCQDs is 6 nm, compared with that of 8 nm in SAQDs. Moreover, the full-width-at-half-maximum of the PL peak of the SCQD sample is 102 meV, which is 11% narrower than that of SAQD sample and attributed to the more uniform QDs on patterned substrates. The integrated PL intensity from the SCQD sample is as strong as that of the reference SAQD sample by taking the dot density into consideration where the dot density on SCQD sample (25 μm^{-2}) is about half of that on SAQD samples. The ratio of integrated PL intensity between 300 K and 77 K remains the same on both SCQD and SAQD samples. This confirms that the optical quality of regrown SCQDs layer on processed samples is comparable to that of SAQDs grown on unprocessed epiready substrates.

2.3.3 Buffer Layer Thickness

Figure 2.9 shows the AFM line scans, which are averaged over five different locations on the same samples, of nanopores prior to QDs regrowth, after atomic hydrogen-assisted cleaning at 480 °C, and after 10-ML, 30-ML, and 50-ML GaAs buffer layer deposition. Prior to and after atomic hydrogen-assisted cleaning, AFM line scans are similar, confirming the preservation of patterns after the desorption process at a lower temperature. With the substrate temperature increased to 500 °C for the deposition of the

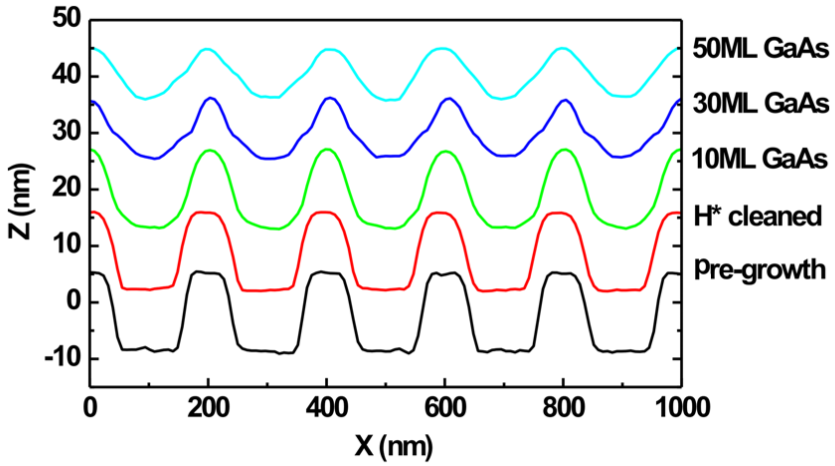

Figure 2.9 AFM line scans of patterned nanopores prior to QDs regrowth, after atomic hydrogen cleaning at 480 °C, and after 10-ML, 30-ML, and 50-ML GaAs buffer layer deposition.

GaAs buffer layers with various thicknesses, the edges of nanopores begin to get blunt and the bottoms filled up, which is quite similar to the evolution of patterns on a microscale reported by Kan *et al.* [26]. The average pore depth decreases from an initial depth of 13.5 nm to 8.5 nm after 50-ML buffer layer deposition, accompanying a sidewall-angle reduction measured relative to the nanopore bottom surface from 25.5 ° to 6.4 °.

Figure 2.10 illustrates the variation of surface morphologies after QDs regrowth as a function of GaAs buffer layer thicknesses. The thicknesses of deposited GaAs buffer layers are 10 ML, 30 ML, and 50 ML corresponding to Figure 2.10(a) to 2.10(c), respectively. For all samples, 3 ML of InAs is grown right after buffer layer deposition and the arsenic overpressure during QDs regrowth is kept at 5×10^{-7} torr. First of all, no QDs are observed on the surface between nanopores, suggesting the growth conditions for SCQDs regrowth are appropriate. Secondly, as shown in Figure 2.10(a), some small

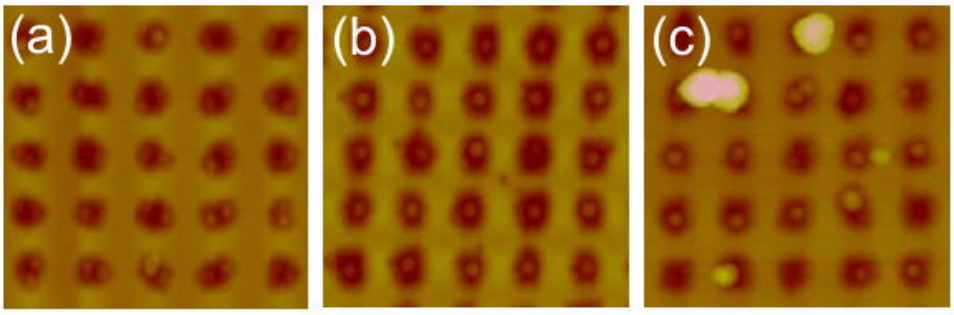

Figure 2.10 AFM images (1 μm × 1 μm) of SCQDs grown with different GaAs buffer layer thicknesses: (a) 10 ML, (b) 30 ML, and (c) 50 ML.

dots are found inside each nanopore if only 10-ML GaAs is deposited prior to QDs regrowth. This result indicates that a thin buffer layer is not enough to smooth out the surface, leading to multiple nucleation sites at the nanopore bottoms, and therefore multiple InAs QDs form accordingly. However, if the buffer layer thickness is increased to 50 ML, overgrown nonuniform QDs, as well as unoccupied nanopores, are observed as seen in Figure 2.10(c). When the average depths of nanopores reduce with increasing buffer layer thickness, the chemical potential difference between the top and the bottom of a nanopore gradually lessens. Eventually, In adatoms will no longer be confined within a nanopore due to insufficient lateral constraint during QDs regrowth [27]. Consequently, In adatoms will migrate to nucleation sites with the least surface energy, rather than be uniformly distributed in each nanopore. Under this circumstance, the uniformity of QDs will be mainly determined by growth parameters, instead of defined patterns. In contrast, when the buffer layer thickness is suitable, small QDs will then coalesce into a single QD due to a preferential migration toward the bottom of the nanopore driven by the surface curvature. As seen in Figure 2.10(b), after deposition of 30 ML GaAs, uniform SCQDs

are demonstrated. Based on this result, a buffer layer thickness of 30 ML is chosen for the rest of this study.

2.3.4 Arsenic Overpressure

Next, the effect of arsenic overpressures on SCQDs and self-assembled QDs (SAQDs) formation is shown in Figure 2.11. Unpatterned epiready GaAs wafers are used as reference samples for SAQD growth and are mounted on the same Mo sample holder alongside the SCQD samples. Both samples are grown under the same growth condition simultaneously. In Figure 2.11(a) and 2.11(d), the arsenic overpressure is 1×10^{-6} torr and the dot density on SAQD sample is 43 μm^{-2}. Although a single dot forms in each patterned site, dot size distribution is broad. On the other hand, when the arsenic

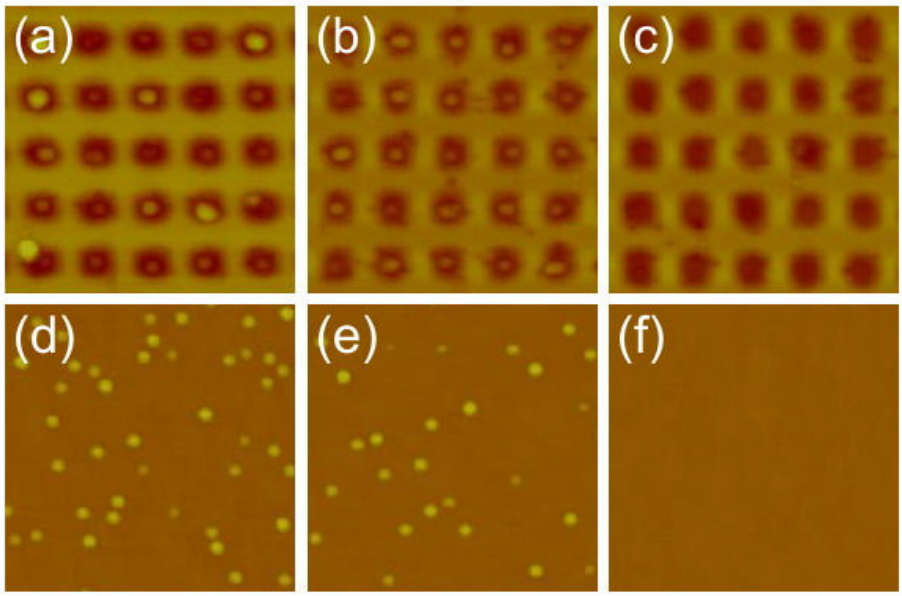

Figure 2.11 [(a)–(c)] AFM images (1 μm × 1 μm) of SCQDs and [(d)–(f)] SAQDs grown at different arsenic overpressures: [(a) and (d)] 1×10^{-6} torr, [(b) and (e)] 5×10^{-7} torr, and [(c) and (f)] 2×10^{-7} torr.

overpressure is decreased to 5×10^{-7} torr, as shown in Figure 2.11(b) and 2.11(e), a lower dot density of 24 μm^{-2} on each SAQD sample is observed. This phenomenon is due to a longer diffusion length of In adatoms on the surface with decreasing arsenic overpressure [28]. Moreover, the increase of diffusion length is also beneficial for more uniform SCQDs, as displayed in Figure 2.11(b). However, if the arsenic overpressure is further reduced to 2×10^{-7} torr, as shown in Figure 2.11(c) and 2.11(f), there is no dot formation on the SAQD sample, while some small dots, which can barely be seen, are formed on the SCQD sample.

PL spectra of uncapped SCQD samples grown at different arsenic overpressures are shown in Figure 2.12. No light emission from the SCQD sample grown at 2×10^{-7} torr is observed, while room temperature PL spectra are detected from those grown at 5×10^{-7} torr and 1×10^{-6} torr. The PL linewidth of the SCQD sample grown at 5×10^{-7} torr is 8 % narrower than that grown at 1×10^{-6} torr and is attributed to the more-uniform QDs formation under lower arsenic overpressure, as observed in Figure 2.12(b). The PL peak positions for SCQDs grown at arsenic overpressure 1×10^{-6} torr and 5×10^{-7} torr are 0.954 eV and 1.008 eV, respectively. The shift of the PL peak position results from the difference in QDs heights grown at various arsenic overpressures. Although the growth temperature and the deposited InAs amount are identical for both samples, higher V/III ratio caused more abundant arsenic atoms to bond with incoming In atoms in the vertical direction and is thus more favorable for taller InAs QDs formation [29], causing a smaller ground-state transition energy. This is also confirmed from the AFM image in Figure 2.11(a), in which several big and irregular dots can be clearly seen under the high V/III ratio growth condition. On the other hand, the integrated PL intensity of the SCQDs

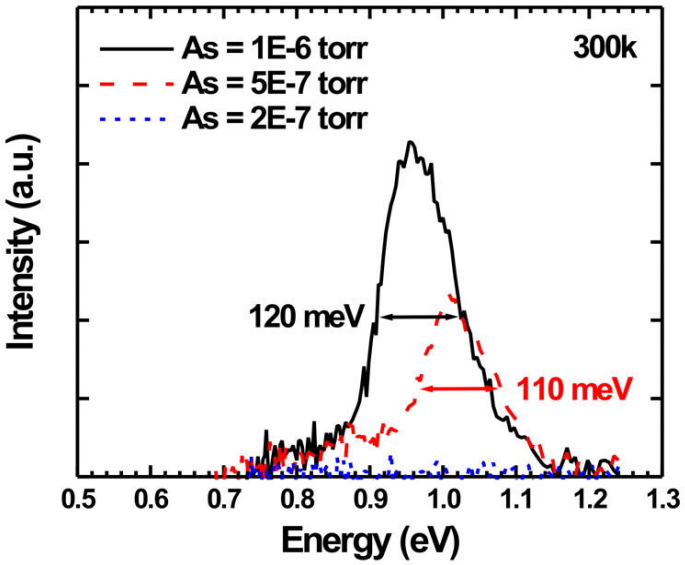

Figure 2.12 Room-temperature photoluminescence spectra of SCQDs grown at different arsenic overpressures: (a) 1×10^{-6} torr (solid line), (b) 5×10^{-7} torr (dashed line), and (c) 2×10^{-7} torr (short dashed line).

grown at 1×10^{-6} torr is about two times higher than that of the SCQDs grown at 5×10^{-7} torr, which requires further investigation. Lastly and most importantly, the PL linewidth from the SCQD sample is narrower than that from the reference SAQD sample, and the integrated PL intensities are comparable under the same growth conditions [30].

2.3.5 Pattern Size

Two sets of samples are fabricated to investigate the influences of the pattern size on the formation of SCQD. The nanopore size histograms of two patterned substrates are shown in Figure 2.13. The depths of nanopores of both samples are 15 nm, and the average sides of nanopores of sample A and sample B are 63 nm and 85 nm, respectively. Sample B, which is fabricated from a standard NIL process, has a more concentrated distribution with a typical standard deviation of 2.9 nm. However, a wider size

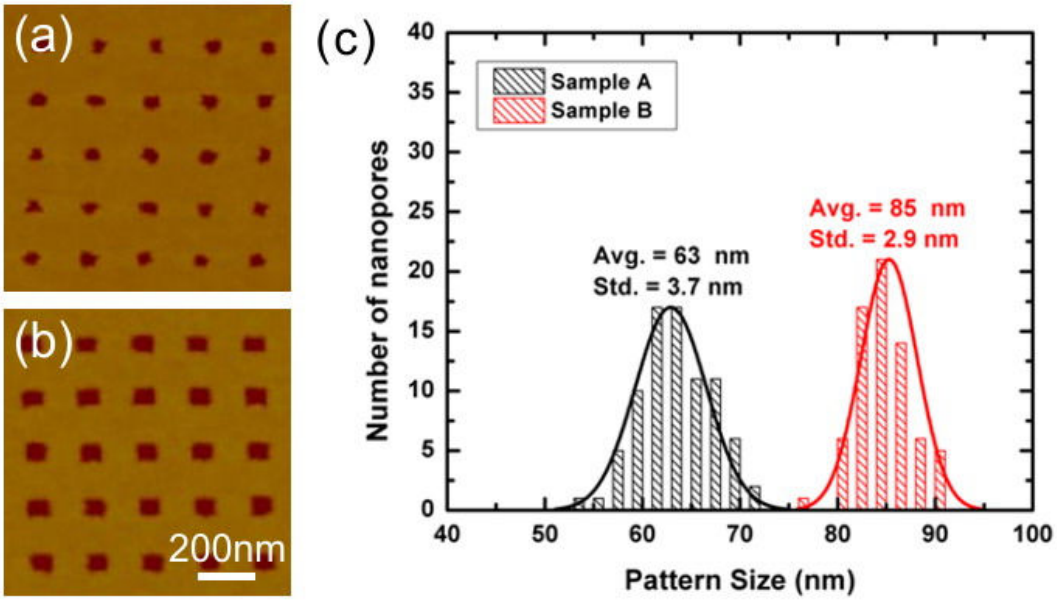

Figure 2.13 AFM images (1 μm × 1 μm) of samples with different nanopore sizes: (a) sample A (63 nm) (b) sample B (85 nm). Corresponding size histograms of sample A and B are shown in (c).

distribution and more irregular edges of nanopores are usually found on sample A. This phenomenon is attributed to process-related imperfections while scaling down the pattern dimension.

After deposition of 30 ML GaAs buffer layer, different amounts of InAs are grown on both sample A and B simultaneously. The critical thickness of InAs on these samples is 2.3 ML under the same growth conditions. Figure 2.14 shows the AFM images of samples after InAs deposition. When 2.5 ML InAs is deposited, multiple-dot occupancy within each nanopore starts to appear on sample B as shown in Figure 2.14(c). With the deposition amount of InAs increasing to 2.9 ML, formation of multiple dots within each nanopore becomes evidently clear as shown in Figure 2.14(d). Further

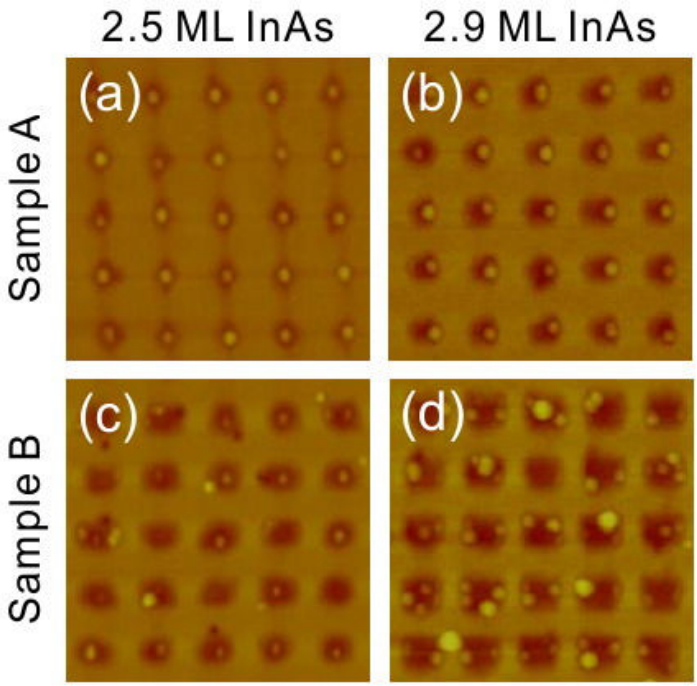

Figure 2.14 AFM images (1 μm × 1 μm) of SCQDs with different amount of InAs: [(a) and (c)] 2.5 ML, and [(b) and (d)] 2.9 ML, grown on two sets of samples with different initial sizes. The average sides of sample A and sample B are 63 nm and 85 nm, respectively.

increasing the amount of InAs deposition promotes the formation of a single large dot through coalition of multiple dots. In contrast, single-dot occupancy in each nanopore is invariably found on sample A despite various deposition amounts of InAs used. These results agree well with what Atkinson *et al.* reported on the size evolution of InAs SCQDs [31]. The dot occupancy appears more sensitive to changes in the pattern size than changes in the amount of InAs supplied.

Figure 2.15 shows the room temperature PL spectra of uncapped SCQD layers grown on samples A and B with different deposition amounts of InAs. Similar to standard self-assembled QDs, inhomogeneously broadened emission is observed in both cases mainly due to the size distribution in the NIL defined nanopores. With the same amounts of InAs deposition, the full-width-at-half-maximum (FWHM) linewidth of

sample A is 100 meV, which is 20% narrower than that of sample B (124 meV). Moreover, the integrated PL intensities of sample A are two to three times higher than those of sample B as well. These superior PL properties are the clear evidence of more uniform SCQD formation, which is consistent with what is observed in Figure 2.14. When the deposition amount of InAs is increased from 2.5 ML to 2.9 ML on either sample, the dots become taller with incorporation of excessive In, leading to a reduction in emission energy. Nevertheless, the amount of red-shift varies depending on single- or multiple-dot occupancy. For samples with smaller nanopores, the pores are largely unfilled with one single dot when 2.5 ML of InAs is deposited. Excessive material will contribute to the increase of dot height instead of dot diameter due to the limitation on the lateral direction. Consequently, the PL peak energy red-shifts more in sample A than in sample B. Besides, while the PL peak energy of sample A decreases with increasing the

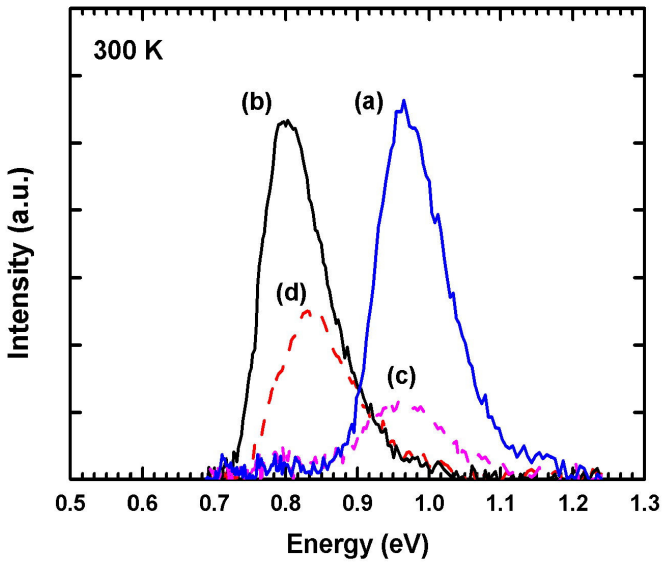

Figure 2.15 Room temperature PL spectra of uncapped single layer SCQDs: (a) 2.5 ML InAs deposited on sample A, (b) 2.9 ML InAs deposited on sample A, (c) 2.5 ML InAs deposited on sample B, (d) 2.9 ML InAs deposited on sample B.

amount of InAs, the peak intensity remains unchanged, suggesting a defect-free layer of SCQDs. This characteristic provides the flexibility of tuning emission energy easily without degrading the quality of SCQDs.

2.4 Capping of Regrown QDs

To incorporate the regrown QDs into device structures, a high quality cap layer is necessary. In addition to lattice matching to the substrate, this layer must have a bandgap larger than that of the regrown QD layer in order to provide sufficient carrier confinement. At the same time, since the growth temperature of InAs is usually lower than those of other materials, crystal quality of the cap layer material at such a lower growth temperature needs to be taken into account. Consequently, the best candidate in our material system is GaAs.

To compare the optical properties of SCQDs and SAQDs after the deposition of a GaAs cap layer, an unpatterned epi-ready GaAs sample is mounted on the same Mo puck along with a patterned GaAs sample as a reference. After oxide desorption, 30 ML GaAs buffer layer and 3 ML InAs are deposited first and 40 nm GaAs cap layer is subsequently grown on both samples. The growth temperature is kept at 500 °C through the growth of all layers. Figure 2.16 shows the AFM surface images and line scans of both samples. Apparently, the surface of the unpatterned GaAs sample is much smoother than its counterpart since there is less topography to smooth out compared to that of the patterned GaAs sample. Without a doubt, the surface morphology of the patterned sample is disappointing. Those large bumps inherently originate from regrown QDs with similar dimensions and shapes. Since the regrown SCQDs are much bigger than SAQDs, greater strain will be introduced to the regrown SCQDs, leading to the formation of misfit

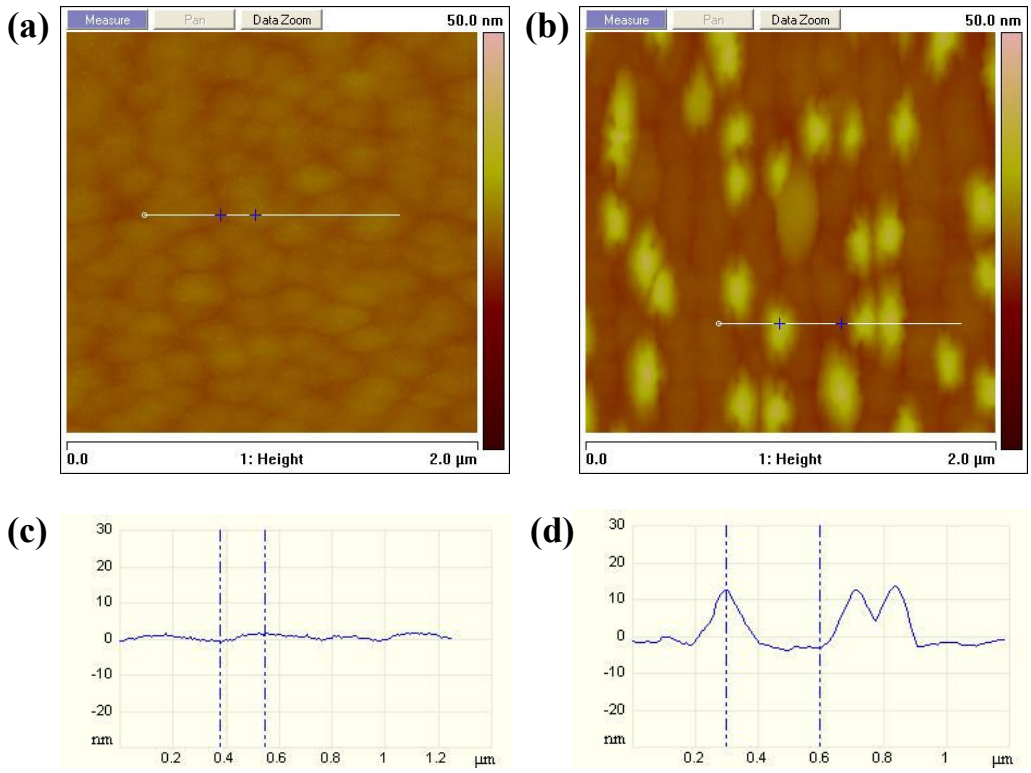

Figure 2.16 AFM images and line-scans of after deposition of 40 nm GaAs cap layer on: [(a) and (c)] unpatterned GaAs reference sample [(b) and (d)] patterned GaAs sample.

dislocation. Once dislocations are formed, random surface undulation might be generated, and eventually results in a rough surface as shown in Figure 2.16 (b).

The PL measurements shown in Figure 2.17 further reveal the optical quality of SAQDs and regrown SCQDs at 300 K and 77 K. At low temperature, the PL spectra of SCQDs and SAQDs are similar to those in Figure 2.8 except for the peak positions and FWHM linewidths. The luminous efficiency of SCQDs is comparable to that of SAQDs. However, the PL of regrown SCQDs is completely quenched at room temperature as shown in Figure 2.17 (a) while the PL intensity from SAQDs is still strong. This confirms the formation of dislocation during the growth of GaAs cap layer. To resolve this issue, a smaller pattern size for regrown QDs is required as suggested in Section 2.3.4.

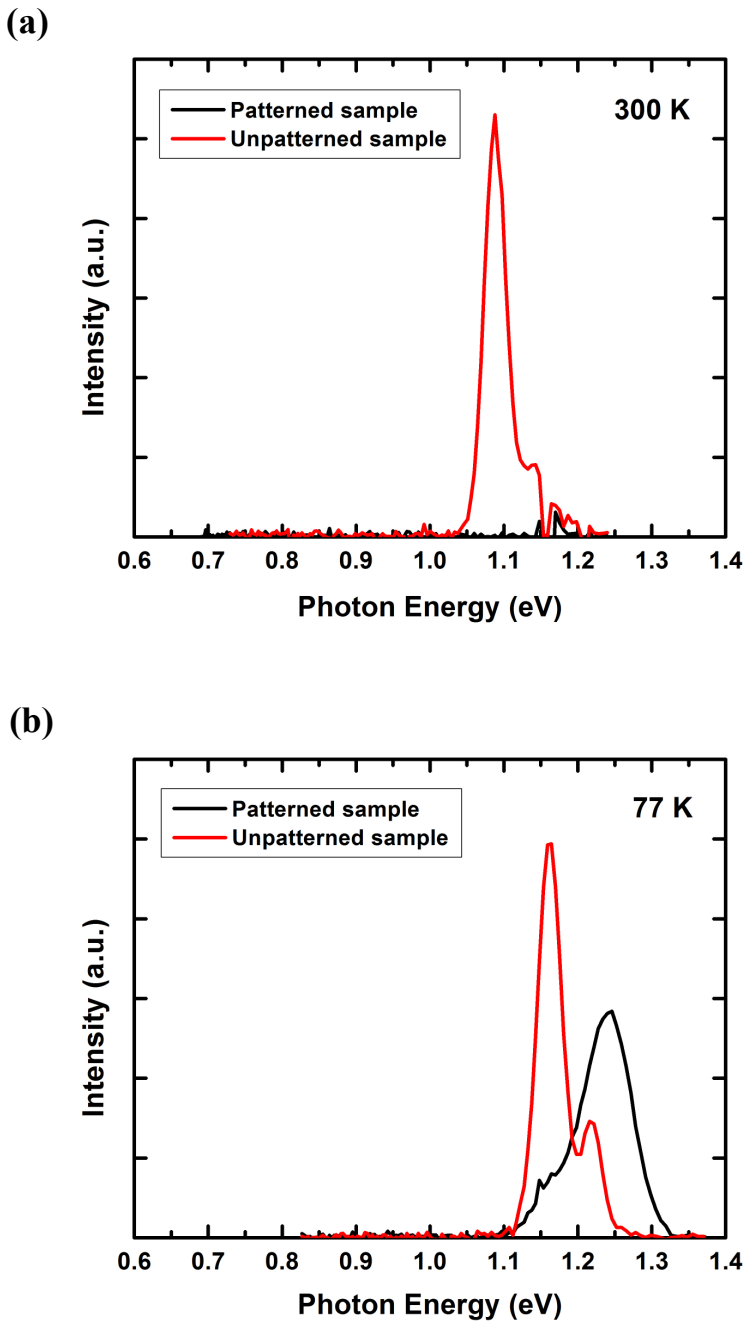

Figure 2.17 PL measured from patterned and unpatterned samples after 40 nm GaAs cap layer deposition at (a) 300 K, (b) 77 K.

To summarize, soft NIL indeed provides an alternative way to pattern the semiconductors without creating potential non-radiative recombination centers. InAs QDs have been successfully demonstrated on GaAs substrate patterned by soft NIL with good uniformity and optical luminescence. These features suggest that using soft NIL technique to transfer nanoscale patterns is an innovative approach of achieving high quality QDs with precise positioning at a low cost and high throughput for device applications. A blemish in the otherwise excellent method is the sensitivity of the optical quality of QDs to pattern size and growth conditions, which requires careful adjustments in process and growth parameters.

With the intention of eliminating this inherent sensitivity of regrown QDs, another top-down approach will be explored in Chapter 3. Strained InGaAs single QW will be first grown by MBE, patterned by soft NIL, and etched into pillar QDs. In this way, optimization will be only necessary for the growth of InGaAs QW on GaAs substrate. Except for the reduction of time for fine-tuning growth parameters, the issue of excessive strain during capping process of InAs regrown QDs is also anticipated to be resolved.

CHAPTER 3 PROCESS DEVELOPMENT OF PILLAR QUANTUM DOTS AND CHARACTERIZATION RESULTS

3.1 Process Development

In order to fabricate pillar QDs and compare them with regrown QDs, a GaAs substrate topped with one or more InGaAs QW is chosen for this study for its maturity to grow and process. Besides, since strained InGaAs QWs on GaAs substrate has been extensively studied for its application in 980 nm lasers [32, 33], it is also important to contrast the performances of QD lasers with existing results at this wavelength.

To start with, the template for the soft NIL must be inverted from pattern of pores to pillars while the rest of the specifications of template remain unchanged. Figure 3.1(a) and 3.1(c) show the AFM images and line scans of the template for pillar QDs, and 3.1(b) and 3.1(d) the PDMS mold made out of the template. Under normal circumstances, the process window for successful pattern transfer is highly relevant to the contrast of the pattern, which is the height difference between the top and the bottom. The higher the contrasts, the wider the process windows. Hence, the specification of contrast is set to be larger than 70 nm. Nevertheless, in Figure 3.1(c) and 3.1(d), it brings to our attention that the height of the pillars on the template is less than 40 nm, and the pores on the PDMS mold are less than 30 nm. Although the contrast is proved to be still good enough for successful imprinting, more rigorous process control have to be introduced.

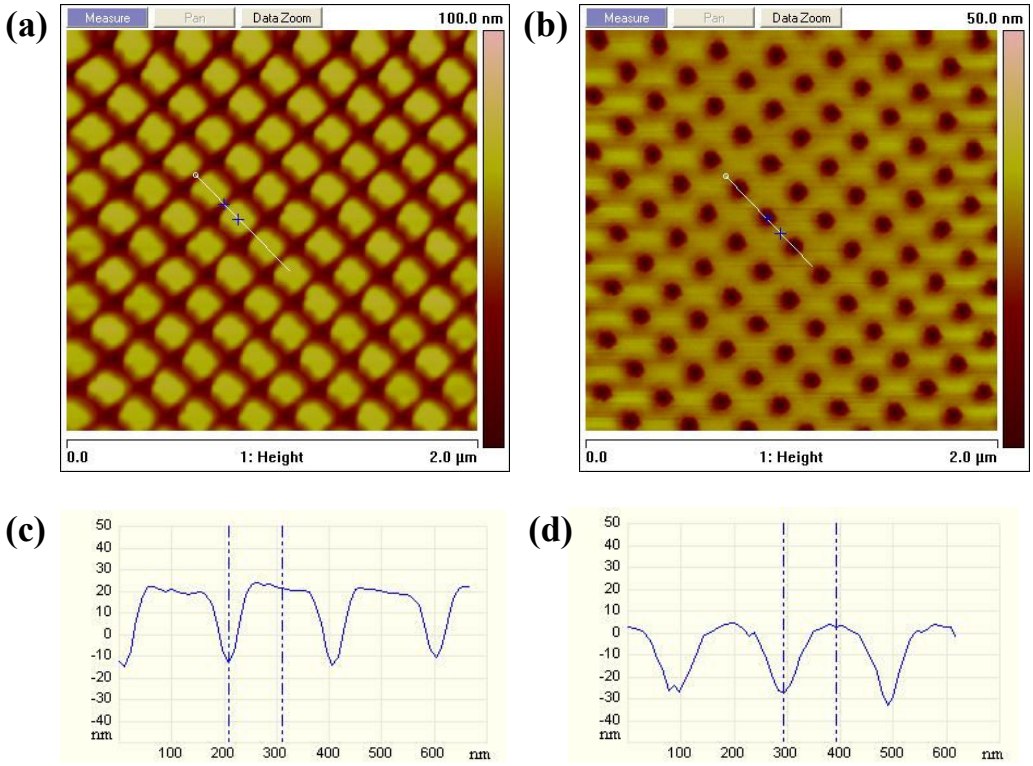

Figure 3.1 AFM images and line scans of [(a) and (c)] the template for pillar QDs fabrication and [(b) and (d)] the PDMS mold which is made from the template.

The first step for the fabrication of pillar QDs is to design a simple InGaAs / GaAs structure that is compatible with the subsequent etching step. Single quantum well structure is easier to grow and generally more suitable for fabricating pillar QDs. If two or more quantum wells are adopted, the interaction between quantum wells might complicate the analysis or results. As for the thickness of cap layer, it depends on the type of etching process. Figure 3.2 shows structures for fabrication of pillar QDs by dry etching and wet etching, respectively. In Figure 3.2 (a), the epitaxial layers consists of a 400 nm GaAs buffer layer, followed a 10 nm InGaAs quantum well, and a 50 nm GaAs cap layer. The thick cap layer is designed to keep the InGaAs QW away from the surface,

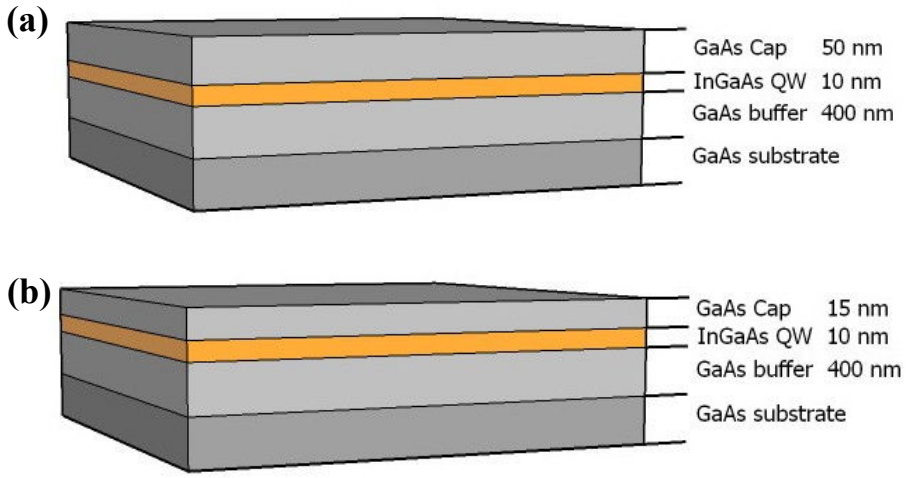

Figure 3.2 Layer structures for the fabrication of pillar QDs using (a) dry etching (b) wet etching.

avoiding any potential damage associated with the dry etching process. As for the structure used in the pillar QDs fabrication by wet etching, the thickness of the cap layer will be decreased to 15 nm in order to etch through the InGaAs QW in a short amount of time. The growth of these structures is performed in a SSMBE chamber, and all layers are undoped with a background doping level below 10^{15} cm^{-3}. The In composition in the quantum well is varied between 0.07 and 0.21 to select the QW emission wavelength to a specific value we are interested in.

Two InGaAs/GaAs multiple quantum well (MQW) structures with different In composition are grown for accurate calibration of the percentage of In in the active region. The (004) high resolution x r-ay diffraction (HDXRD) rocking curves of the samples are measured using a highly monochromatic Cu $K_{\alpha 1}$ x-ray beam conditioned by 4 bounces through Si <022> channel cut crystals. The rocking curves of the samples are shown in Figure 3.3, and the compositions of In are simulated to be 0.12 and 0.18, respectively.

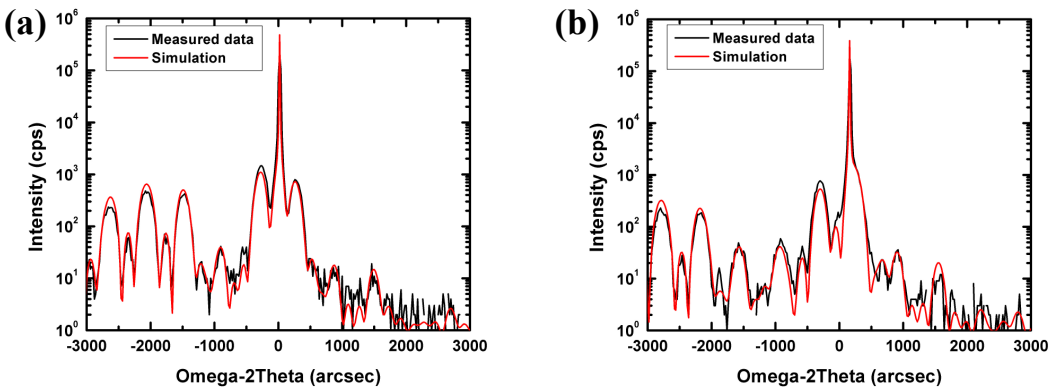

Figure 3.3 Measured (black line) and simulation (red line) rocking curve of InGaAs/GaAs MQW structure: (a) $In_{0.12}Ga_{0.88}As$ MQW, (b) $In_{0.18}Ga_{0.82}As$ MQW.

Optical qualities of these MQW samples are displayed in Figure 3.4. For $In_{0.18}Ga_{0.82}As$ MQW samples, the luminous properties are better than those of $In_{0.12}Ga_{0.88}As$ MQW samples due to better carrier confinement in the QW. Other than that, all the spectra show strong intensity and pretty narrow FWHM linewidths at 300 K, indicating the growth conditions are optimized.

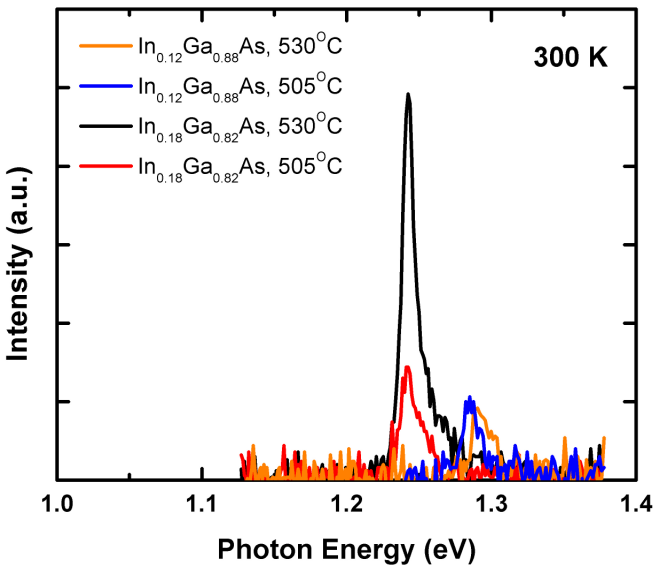

Figure 3.4 PL comparison of InGaAs/GaAs MQW structures grown at different substrate temperatures.

Using the structure mentioned above, soft NIL is performed on the samples following the same procedures described in Chapter 2. After the preparation of the samples is completed, pillar QDs can be formed by either dry etching or wet etching through the QW layer.

3.1.1 Dry-Etched Pillar QDs

Unlike previous work done on InP substrate [34], dry etching of InGaAs/GaAs is a relatively easy task. The dry etching could be performed in room temperature with acceptable surface morphology. Meanwhile, since the selection ratio between InGaAs/GaAs and silicon nitride is greater than 10, the thin silicon nitride layer used in the soft NIL serves not only as the sacrificial layer, but also the etching mask for dry etching. Therefore, using metal as etching mask in the InP case is not necessary. Inductively coupled plasma reactive ion etching (ICP-RIE) is selected to etch through the InGaAs QW into pillar QDs in this study. Due to the separate control over the ion energy and ion density, the ICP-RIE etching can generate high density plasma to achieve anisotropic

Table 3.1 ICP–RIE recipe for the etching of InGaAs / GaAs pillar QDs

ICP-RIE etching condition	
SiCl	1 sccm
Ar	5 sccm
Pressure	1.5 torr
RF power	30 W
ICP power	60 W
Etch time	60 sec
Temperature	25 °C

etch with low damage to the semiconductor, and thus suitable for the dry etching of pillar QDs. Nevertheless, the etch-induced damage to the semiconductor is still a concern [35].

The etch recipe uses the gases $SiCl_4$ and Ar, and the etching rate for GaAs is estimated to be 1.5 nm/s. RF power is controlled to be as low as possible to minimize bombardment damage while large enough to keep the sidewall straight. Detailed parameters for pillar QDs etching are listed in Table 3.1.

After being loaded into the ICP-RIE chamber, the samples undergo a short oxygen plasma etch treatment to help remove residual organic contamination, and then the recipe in Table 3.1 is run for 60 sec. Figure 3.5 shows the top-view and side-view SEM images of the dry-etched pillar after the silicon nitride layer is removed. The etching depth is 100 nm while the sidewalls are straight, which results from good balance between the RF power and ICP power.

Afterwards, a short wet etching is performed immediately after the ICP-RIE etching to remove damaged layer from the sidewalls of the pillar QDs. A solution

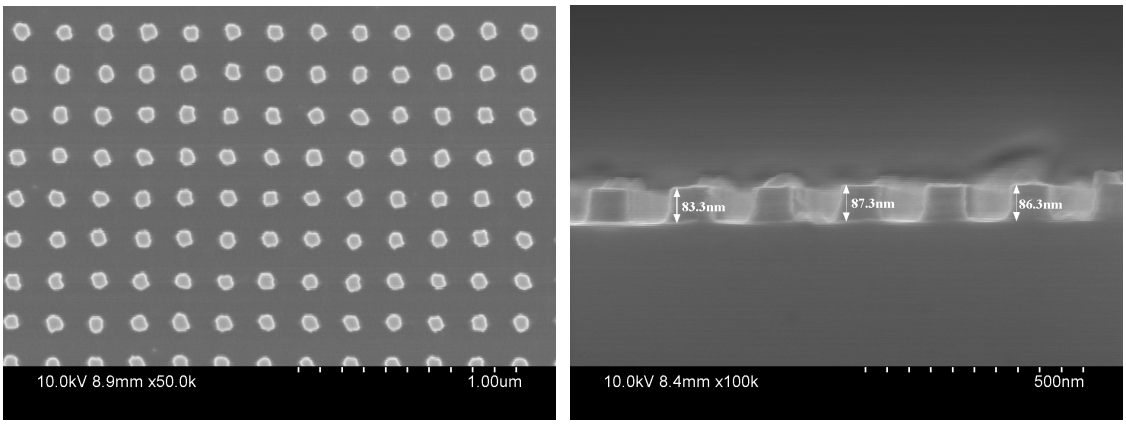

Figure 3.5 The SEM images of InGaAs / GaAs pillar QDs fabricated by ICP-RIE dry etching: (a) top-view, (b) side-view.

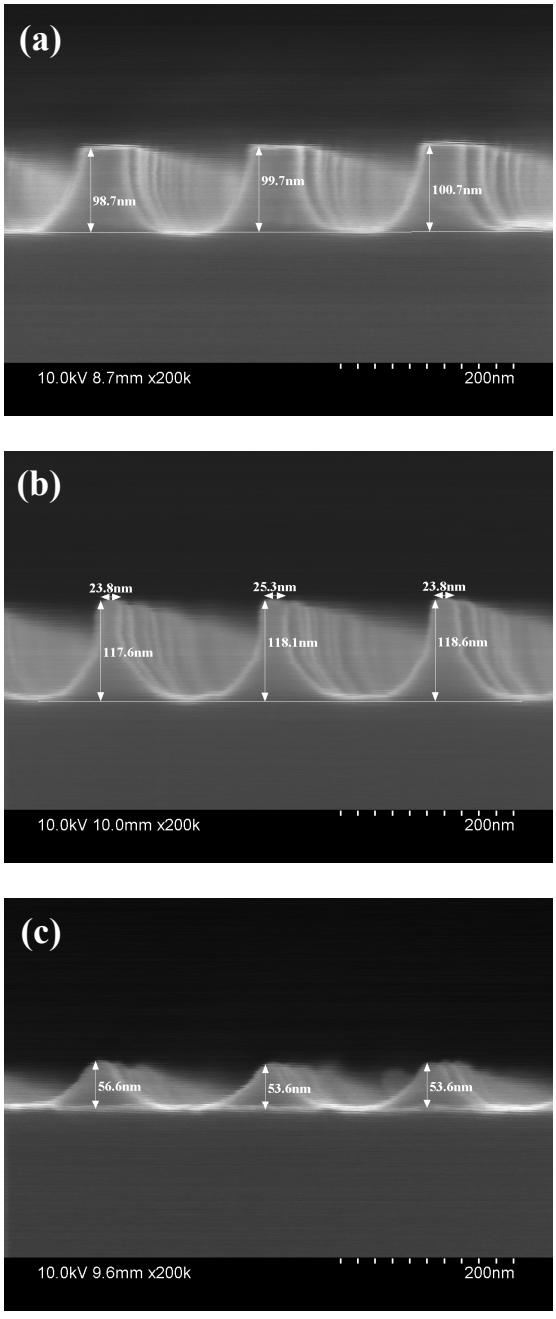

Figure 3.6 The SEM images of InGaAs / GaAs pillar QDs with different wet etching time: (a) 1 min, (b) 2 min, (c) 3 min.

of ammonium, hydrogen peroxide, and deionized water mixture is used for wet etching.

The mixture of the solution is 1:1:790 $NH_4OH:H_2O_2:H_2O$ with a nominal etching rate of

18nm/min. The morphology change with different wet etching time is shown in Figure 3.6. The radii of InGaAs quantum boxes (QBs) will decrease with etching time; nevertheless, if a longer etching time is selected, the QBs will face the risk of completely being etched away as suggested in Figure 3.6(c). Although the morphology is satisfactory, inevitably the PL from pillar QDs is significantly weakened compared to that of the starting QW. Eventually, dry etching method is abandoned for the fabrication of pillar QDs.

3.1.2 Wet-Etched Pillar QDs

In contrast to dry etching, wet chemical etching most likely produces no dead layers at the open sidewalls of the nanostructures. Accordingly, to maintain the optical quality of the embedded active medium, wet etching is inevitably chosen to prevent the material from potential contact of any high-energy particles. For InGaAs / GaAs etch, the etch chemistry is based on ammonium hydroxide, and the mixture of the solution is 1:1:790 $NH_4OH:H_2O_2:H_2O$. The nominal etching rate is 18 nm/min, which promotes good repeatability of the wet etching process. Nonetheless, the isotropic property of wet etching imposes a limitation on the height and morphological control of the pillar QDs. Since the chemical will isotropically etch away the material underneath the etching mask, the maximal height of pillar QDs will be limited by the initial mask size. For dimension of mask is 100 nm, the maximum pillar height is estimated to be 50 nm. If a thick cap layer of 50 nm above InGaAs QW is adopted, the QW will not be etched through before the etching mask is lifted off. Based on this fact, the thickness of GaAs cap layer is revised to be 15 nm to move the QW closer to the surface. Unlike the pillar shape

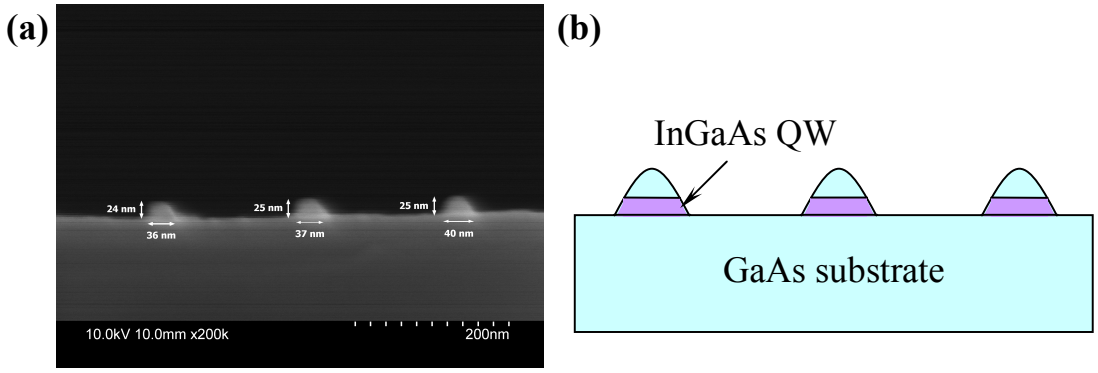

Figure 3.7 Cross-sectional SEM image and schematic diagram of pillar QDs after wet etching is performed for 60 s.

obtained from dry etching, the wet-etched pillar QDs are more pyramidal as show in Figure 3.7(a). The sample is etched for 60 s, and the upper part of pillar QDs shrinks laterally by the amount or 36 nm, which is twice of the etching depth. By this method, the dimension of active material could be adjusted in size with different wet etching time. Noticeable quantization effect will start to appear in the lateral direction once the sizes of the pillar QDs are smaller than 50 nm.

3.2 Characterization Results

Carrier confinements in the InGaAs pillar QDs are similar to those of particles in an infinite potential well, which is provided by the air at the edge of the pillar QDs. By neglecting influences of other effects, such as surface depletion, surface oxidation, or contamination, etc., we could roughly estimate the energy shift due to reduction of the lateral dimension of the pillar QDs in the wet etching process. Although this calculation oversimplifies the realistic situation, it does provide a general guideline to analyze the experimental data. The basic equation used in the calculation is

$$\Delta E = \frac{\hbar^2 \pi^2}{2m_e^*}\left[\left(\frac{n_x}{a}\right)^2 + \left(\frac{n_y}{a}\right)^2\right] + \frac{\hbar^2 \pi^2}{2m_h^*}\left[\left(\frac{n_x}{a}\right)^2 + \left(\frac{n_y}{a}\right)^2\right] \quad (3.1)$$

In Equation (3.1), m_e^* and m_h^* are the effective mass for the electrons and holes in the InGaAs QW, respectively. We assume low-level injection and set all n_x and n_y to 1 in the calculation. The emission energy thus corresponds to the transition between the lowest quantum states (1e-1hh) of the pillar QDs. By assuming separable vertical and lateral quantization, the relation between the emission energy shift and the lateral size of the pillar QDs is plotted in Figure 3.8. Good agreement between the theoretical and experimental values of energy shifts with respect to the dot diameters was reported previously under similar designs and processes to fabricate InGaAs / GaAs pillar QDs [36, 37].

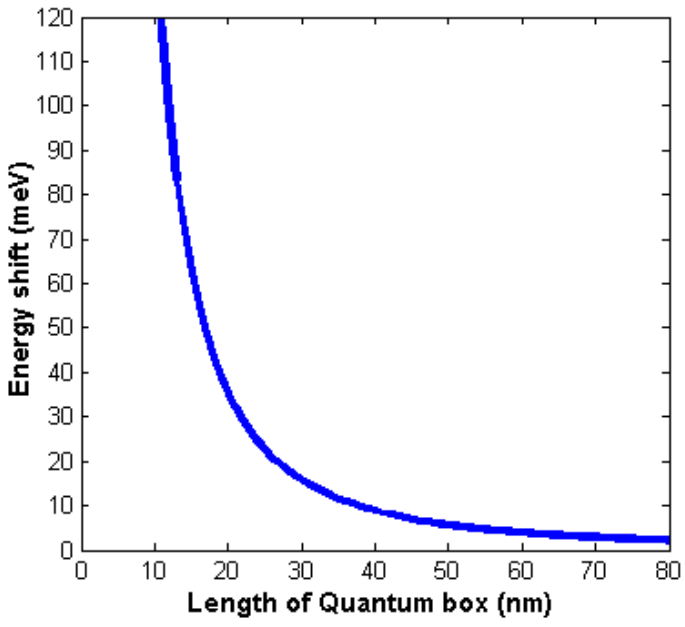

Figure 3.8 Emission energy shift as a function of the lateral size of InGaAs pillar QDs.

The samples used in the series of wet etching experiments are strained InGaAs / GaAs single QW (SQW) as depicted in Figure 3.2(b). After the samples are grown, HDXRD measurements are performed, and the results are analyzed and simulated by computer software to extract the values of the QW thicknesses and In compositions in the QW. Table 3.2 summarizes all the information of the samples for the study of pillar QDs, including In composition, QW thicknesses, and peak emission energy at 77 K.

Table 3.2 Information of InGaAs / GaAs SQW used for the study of pillar QD

Batch no	In composition	QW thickness (nm)		Peak energy @ 77 K
	%	Nominal	Simulated	eV
sv2846	7.5	10.0	7.5	1.446
sv2849	18.4	10.0	9.9	1.296
sv2861	22.0	10.0	9.9	1.250

However, the PL results from our experiments are quite different from what other groups obtained. Figure 3.9 shows the 77 K PL spectra from sample sv2846 with different wet etching time. The peaks located at 1.507 eV are from the GaAs substrate, and the error in PL measurement is estimated to be within ± 3 meV, which is acquired from the peak positions of the GaAs substrate measured for ten times. Surprisingly, the emission energy peaks from all the wet-etched samples are centered at 1.379 eV, and remain unchanged with various etching time. Meanwhile, a large red-shift of 65 meV from that of the as-grown QW is also observed. The FWHM linewidth is about 7 meV, and found consistently narrow among all the samples. Additionally, despite the fact previous work showed orders of magnitude reduction in the PL intensity [38], which was

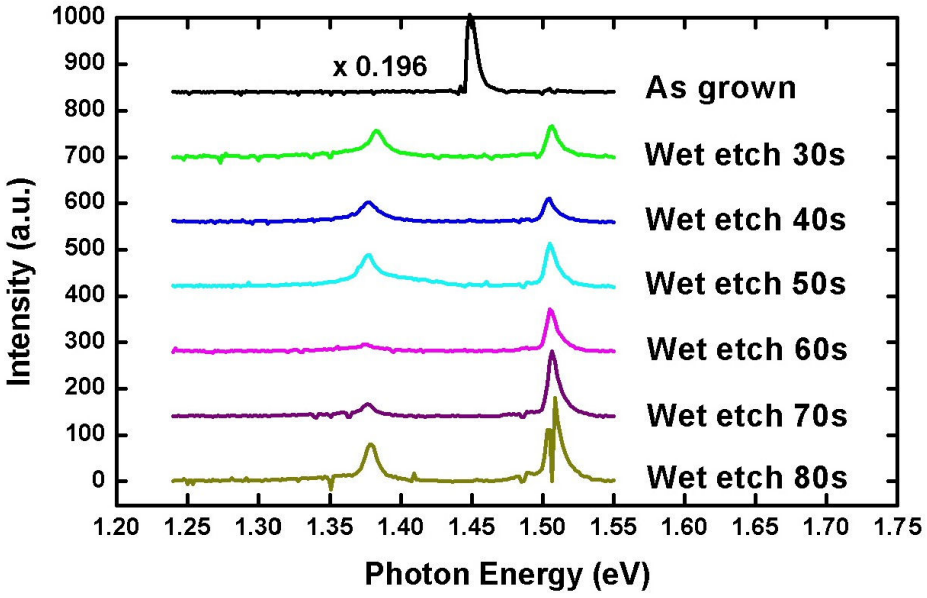

Figure 3.9 77 K PL spectra of etched pillar QDs from sample sv2846 with different wet etching time. The active layer in sample sv2846 is a 7.5 nm $In_{0.075}Ga_{0.925}As$ QW.

attributed to the loss of PL intensity to nonradiative recombination at the open sidewalls for small dots, the PL intensities from sample sv2846 with different etching times remain strong. Similar results are also discovered in sample sv2849 and sample sv2861 except that blue-shift and no-shift in PL peak positions are observed, respectively.

From the results above, extra work has to be done to investigate the discrepancies between the theory and experimental data. Since there might be strain relaxation involved in the etching process of InGaAs and GaAs, the first step is to understand the effects of strain relaxation during wet etching.

From the theory of semiconductor physics, we know the strain plays an important role in affecting the emission energy of a QW. As a result, to gain more insight into this issue, an experiment is conducted to investigate the impacts of strain relaxation on the emission energy shift. The compressive strain in InGaAs QW increases with In composition when InGaAs QW is sandwiched between the GaAs cap layer and substrate.

Hence, by selectively etching away the GaAs cap layer from an InGaAs QW, we might be able to mimic strain relaxation process and evaluate the influence by PL measurements. Sample sv2861 is selected for this experiment for its high In composition in the QW, on which selective etching of GaAs over InGaAs will occur.

Figure 3.10 shows the emission energy shift and normalized PL intensity (with respect to the as-grown QW sample) with various wet etching times. For shallow etch (etch time < 40 s), the emission peaks barely move, but the intensities begin to drop by an order of magnitude for 40 s etch owing to the introduction of additional surface states. Due to a much slower etching rate of InGaAs by ammonium hydroxide solution when the In composition is larger than 20 %, selective etching of GaAs over InGaAs is achieved. As the etching time is longer than 60 s, the GaAs cap layer is completely etched away, and a blue-shift of as much as 25 meV is observed. On the other hand, the PL intensity also degrades significantly due to the increase of nonradiative recombination via the surface states as the surface gets rougher with longer etching time. In fact, this blue-shift is a combination effect of strain relaxation, surface oxidation, and the enhancement of energy level due to a higher surface potential (i.e. air) [39]. So, blue-shifts of 25 meV in the emission energy could be used as a reference value to estimate the influence of strain relaxation. Using this reference, the effect of strain relaxation is actually much less in the wet etching of sample sv2846 since the strain between InGaAs QW and GaAs is merely 0.5 %, compared to 1.6 % in sample sv2861. Besides, a larger red-shift, instead of blue-shift, in the emission energy is found in sample sv2846. For this reason, strain relaxation is obviously not the mechanism behind the phenomenon.

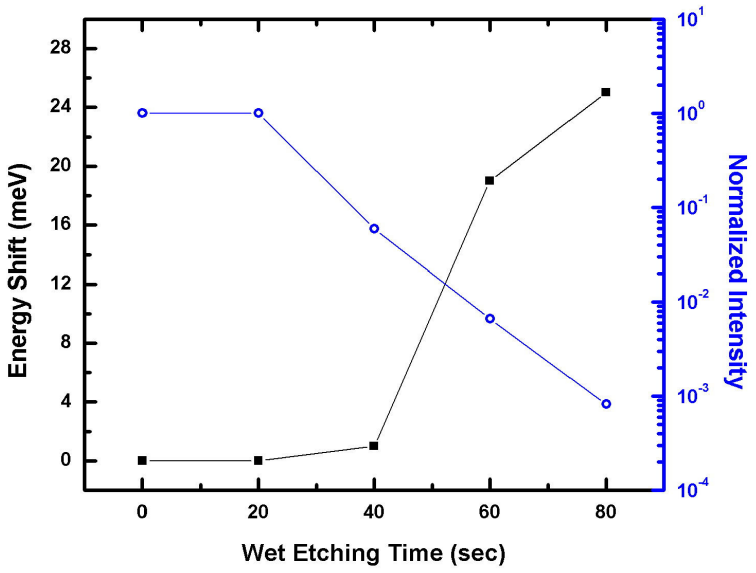

Figure 3.10 Emission energy shift and normalized PL intensity (to the as-grown QW sample) variation as functions of wet etching time. The sample used is the as-grown wafer of sv2861, and the nominal wet etching rate is 18 nm/min.

So far, there is no plausible explanation for the red-shift of the emission wavelength in sample sv2846 to the best of our knowledge. Consequently, while more experiments await to be carried out to investigate the physics behind this abnormal phenomenon, we try to propose a model in an attempt to explain all the experimental results consistently in the following section.

3.3 Quantum Structure Lattice

3.3.1 Model Description

Periodic structures are commonly used in the semiconductor devices to provide optical deflection in a specific direction. For instance, one-dimensional corrugated

grating is formed in the GaAs active region in the first distributed-feedback (DFB) laser [40]. In order to maintain the phase coherence of the plane wavefront and avoid destructive interference, the Bragg relation, which is given in Equation (3.2), must be fulfilled.

$$\Lambda = \frac{m\dfrac{\lambda_0}{n_{eff}}}{2}, m = 1, 2, 3\ldots \tag{3.2}$$

where Λ is the periodicity of the grating, λ_0 is the optical wavelength in the free space, and n_{eff} is the effective refractive index for the mode under consideration. Under such a circumstance, the grating itself only serves to provide desired Bragg scattering. It does not emit light, and the spontaneous emission is still dominated by the optically active medium. However, one way to change the spontaneous emission characteristics, as suggested by Purcell [41], is to change the environment surrounding of the optoelectronic emitters. If the emitters, in the form of QWs or QDs, are placed between reflectors, the spontaneous emission characteristics in the emitters could be enhanced or inhibited by manipulating the density of associated electromagnetic states. Cavities formed by photonic crystal [42, 43], distributed Bragg reflector (DBR) [44, 45], DFB [40, 46], and optical waveguide [47], have been extensively adopted in the past for this purpose.

Therefore, by analogy to the concept mentioned above, it is possible to have similar results from the 2-D array of pillar QDs fabricated in this work. When the periodicity of the array is an integer multiple of the half wavelength of the optical emission from the pillar QDs, such a 2-D QD array, termed quantum structure lattice (QSL), becomes a high-Q cavity in the plane of emitters through the constructive optical interaction due to the Bragg scatterings.

Figure 3.11(a) shows an SEM image of the 2-D QD array and the corresponding schematic diagram. The distance a between the pillar QDs is 200 nm, and two arbitrary lattice points of (2,5)a and (5,2)a with the same distance *d* from the origin (0,0) are chosen in Figure 3.11(b) to help illustrate how the spontaneous emission characteristics are controlled in the QSL. When the inter-QD distance *d* is an integer multiple of the emission half wavelength as described in Equation (3.2), the Bragg condition is satisfied, and the light emitted from the origin point (0,0) will constructively interfere with the nearest neighboring emitters located at *d*. The process iterates, making the whole QD array a high-Q cavity. This is quite similar to the reflection high-energy electron diffraction (RHEED) of semiconductor surface molecules in a molecular beam epitaxy (MBE) system [48]. As a result, the wavelength of the light emitted from the QSL could be manipulated by adjusting the inter-QD distance *d*. Nevertheless, due to a fixed *d* in the template for pillar QD fabrication, λ_0 is changed instead by varying the In composition and QW thickness in the SQW. The same results are expected if the emission wavelength of QW is properly chosen.

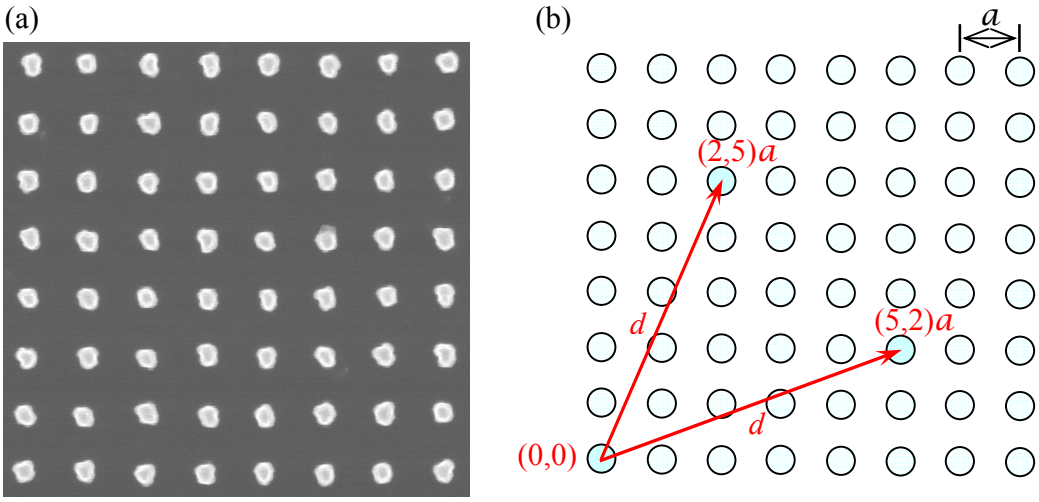

Figure 3.11 (a) SEM image of the InGaAs / GaAs pillar QD array. (b) Square QSL model shown an inter-QD distance *d* between origin and two lattice points (2,5)*a* and (5,2)*a*. which fulfills the Bragg condition.

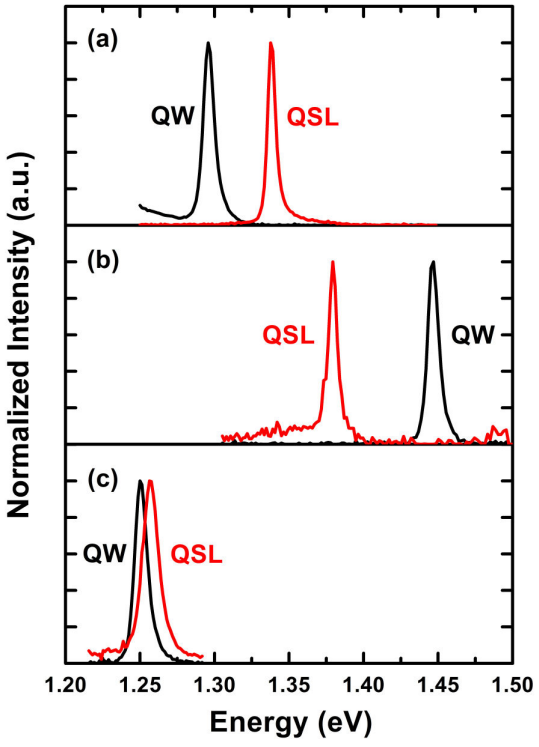

Figure 3.12 Normalized PL spectra (77 K) from the strained InGaAs QWs and the QSL fabricated from the same material. (a) sv2849: 10 nm $In_{0.18}Ga_{0.82}As$ / GaAs QW, (b) sv2846: 7.5 nm $In_{0.075}Ga_{0.925}As$ / GaAs QW, (c) sv2861: 10 nm $In_{0.22}Ga_{0.78}As$ / GaAs QW.

3.3.2 Experimental Verification

Figure 3.12 shows the normalized 77 K PL spectra from the strained InGaAs QWs and the QSL fabricated from the same material. The samples are sv2849, sv2846, and sv2861 in Figure 3.12(a), 3.12(b), and 3.12(c), respectively. Table 3.3 summarizes the experiment results in Figure 3.12, including the average diameter of the pillar QDs, the PL peak shifts between the QSL sample and the as-grown sample, and the PL FWHM linewidths of the QSL samples.

Batch no	Average diameter of QBs	PL peak shift		PL FWHM linewidth	Calculated	
	nm	Type	Amount (meV)	meV	*m*	nearest neighbor positions
sv2849	38	blueshift	39	8	8	*(±1,±3)a, (±3,±1)a*
sv2846	29	redshift	65	7	5	*(±2,±5)a, (±5,±2)a*
sv2861	50	blueshift	6	12	2	*(±1,±1)a, (±1,±1)a*

Table 3.3 Summary of the experimental data in Figure 3.12, and the calculated *m* and the nearest neighbor positions which fulfilled the Bragg conditions.

In Figure 3.12 (a), the PL peak of sv2849 (1.335 eV) is not located at the same position of the as-grown QW sample (1.296 eV). The PL peak of the QSL sample is blue-shifted by 39 meV from that of the QW sample while maintaining a narrow FWHM width. Since the average diameter of etched QBs is about 38 nm, the in-plane quantum size effect should not contribute significantly to the large blue shift. The calculated integer *m* that fulfills the Bragg condition is 8 and the nearest resonant neighbors are located at (±2,±5)*a* and (±5,±2)*a* of the QSL from the origin. In sv2846, with an average QB diameter of 29 nm, the 77K PL spectrum shows a peak centered at 1.382 eV in Figure 3.12 (b), which is 65 meV red-shift from that of the as-grown QW sample (1.447 eV). Again, the QSL sample maintains a narrow PL spectrum with a FWHM near 7 meV. The calculated integer *m* that fulfills the Bragg condition is 5 and the nearest resonant

neighbors are located at (±1,±3)*a* and (±3,±1)*a*. Then, a third QSL sample, sv2861, is engineered such that the spontaneous emission peak position will be the same as the as-grown QW sample. In this sample, the designed QSL emission wavelength is ~1.26 eV (at 77K) which gives an $m = 2$ and the nearest neighbors are located at (±1,±1)*a*. As shown in Figure 3.12(c), the 77K PL spectrum of the QSL is almost identical to that of the as-grown QW with only a 6 meV blue-shift. The small emission energy difference mainly comes from the grown QW structure deviated from the designed material parameters and the refractive index value used [49]. Nevertheless, the QSL concept has clearly demonstrated that the in-plane Bragg diffraction plays an important role in addition to the 1-D quantum size effect in a properly designed and fabricated QSL array structure.

Although the results support the proposed model plausibly, the physics behind the phenomenon remain unexplained. So, analysis of the data is necessary to fully understand the mechanism of the QSL. In Figure 3.12(a), because the average of InGaAs pillar QDs is about 38 nm, the quantum size effect does not appreciably contribute to the blue-shift of the PL peak in the QSL sample. Since the long-wave TO and LO phonon energy in GaAs at 77 K is 33.67 meV and 36.46 meV, respectively [50], the blue-shift of the PL peak energy might be achieved by the absorption of an LO phonon. In contrast, two TO phonon emissions are involved in the red-shift of the PL peak energy in Figure 3.12(b). As in Figure 3.12(c), the peak from the QSL sample is almost identical to that of the as-grown QW with only a 6 meV blue-shift, and the emission is mainly due to QW ground state transition. This spontaneous emission behavior can be explained in terms of phonon-assisted optical transitions.

3.3.3 Regrowth over QSL Structure

In photonic crystal theory, the periodic refractive index change will create photonic stop band, limiting light propagation along certain directions. As a consequence, to distinguish the fundamental principle of QSL from that of photonic crystal structures, the large periodic index change between the air and semiconductor in this study needs to be removed to verify the validity of the QSL model. This task could be achieved by regrowing GaAs cap layer over the entire QSL structure.

A sample similar to sv2849 is fabricated, loaded into the MBE chamber, and covered with 50 nm GaAs after standard atomic-hydrogen-assisted desorption. The emission peak wavelength is compared to see whether the peak deviates after the index change is eliminated. The 77K PL spectra are shown in Figure 3.13. First, as expected, a blueshift of ~ 30 meV from the PL peak of the as-grown QW is observed after the fabrication of QSL sample if Figure 3.13 (a) and (b) is compared. Notwithstanding, the QSL peak positions are almost identical before and after the growth of a thick GaAs cap layer as shown in Figure 3.13 (b) and (c). Supported by this result, the QSL model is believed to be the ruling mechanism of what has been observed.

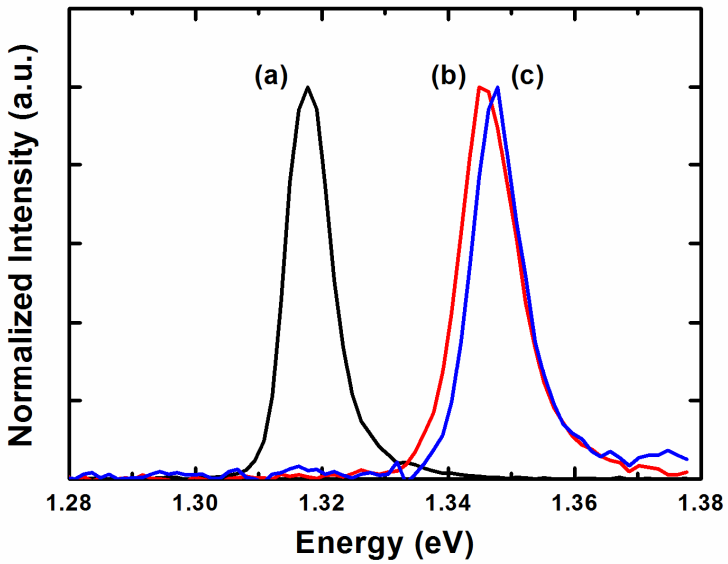

Fig. 3.13: PL spectra (77K) comparison between (a) as-grown 10 nm $In_{0.18}Ga_{0.82}As$/GaAs QW, (b) as-processed QSL from (a), and (c) QSL from (b) with a 50 nm regrown GaAs cap layer.

3.4 Characteristics of QSL

3.4.1 Temperature Dependency of Emission Peak Wavelength

Temperature dependence of spontaneous emission wavelength of semiconductor is essentially determined by band-gap energy variation. However, this undesired temperature-sensitive property could only be mitigated by limited approaches. The most prevalent approach is to incorporate microcavities, such as DFB or DBR, with light emitters, less temperature-sensitive results were frequently reported [51, 52]. Nevertheless, the passive microcavities only served to provide necessary Bragg scatterings/reflections; the spontaneous emission was still dominated by the emitter itself. And, the improved performance comes at the cost of sacrificing output power and

increasing process complexity. Alternatively, the other approach is to utilize the strain effect between the active medium and surrounding material to inhibit temperature dependence [53, 54].

Since the emission peak wavelength of QSL is determined by Bragg conditions of the 2-D QB array and the refractive index of QW, its temperature dependence is expected to be similar to that in DFB structure. Nevertheless, the temperature insensitivity property in DFB structure was only observed under stimulated emission operation due to weak coupling of the higher order grating and the evanescent optical field. In contrast, if Bragg condition is fulfilled, the lattice points of the QSL structure and the QB array are coupled tightly. Thus, the shift of the emission peak wavelength of a QSL is expected to be less sensitive than a QW structure as the surrounding temperature varies. As shown in

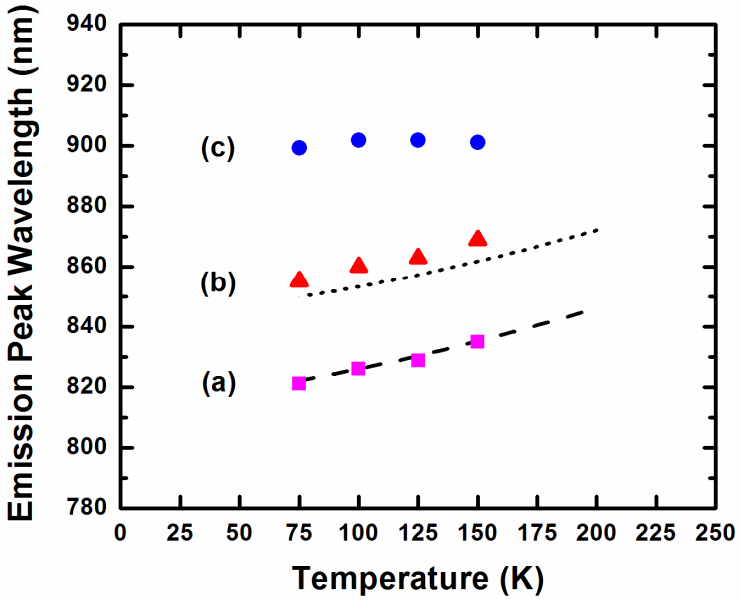

Figure 3.14: Temperature dependence of the spontaneous emission peak wavelength of (a) GaAs substrate, (b) InGaAs SQW, and (c) QSL. The dashed and dotted lines are calculated GaAs and InGaAs QW energy-gap values between 77 and 200K, respectively.

Figure 3.14, the temperature dependence of the spontaneous emission wavelength of a QSL between 77 and 150 K is 0.024 nm/K. In comparison, the emission wavelength of the reference InGaAs QW changes at a rate of 0.177 nm/K in the same temperature range. As expected, the emission peak wavelength of a QSL is predominately determined by Bragg conditions of the 2-D QB array and its temperature dependence on the diffractive index of the QW, similar to a DFB structure.

Figure 3.15 shows the PL spectra of sample sv2846 measured as a function of temperature. When temperature increases, the peak of GaAs substrate moves following the band-gap energy variation with temperature. On the other hand, the peak of QSL hardly moves, and remains centered at 900 nm between 77 K and 150 K. The PL peak intensities from QSL arrays decrease rapidly while the temperature is ramping up. Although it is known that nonradiative recombination at the etched surface of GaAs is usually accounted for degraded PL intensities in enhanced temperature range, another factor also plays a role. When the temperature surrounding the QB arrays increases, the peak emission wavelength gradually red-shifts due to the band-gap shrinkage of InGaAs QBs. Consequently, only part of the total spontaneous emission contributes to the phonon-assisted emission/absorption process, which leads to a reduction in PL intensity from the QSL. Once the Bragg condition could not be satisfied, the control over spontaneous emission properties of the QSL is no longer sustainable. Therefore, for temperature above 150 K, the PL intensity from the QSL is too weak to be observed. Nonetheless, due to a low array density of the pattern used in this study, most of the active region is etched away when etched pillars are formed. The intensity from the QSL can be improved by optimizing the dimension of the QBs and the pitch between them.

Meanwhile, since the average diameter of etched pillars containing InGaAs QBs is about 30 to 50 nm, the in-plane quantum size effect is small compared to that in the growth direction. Hence, even though imperfection of the fabrication process results in non-uniformity in the lateral size of QBs, the FWHM linewidths from the QSL is still close to those from as-grown QWs. On the other hand, the constructive interaction between neighborhood QB emitters is also beneficial for the reduction of FWHM linewidths. Generally, the average FWHM linewidth of the QSL is about 7 to 13 meV at low temperature range, which is comparable to those obtained using other techniques.

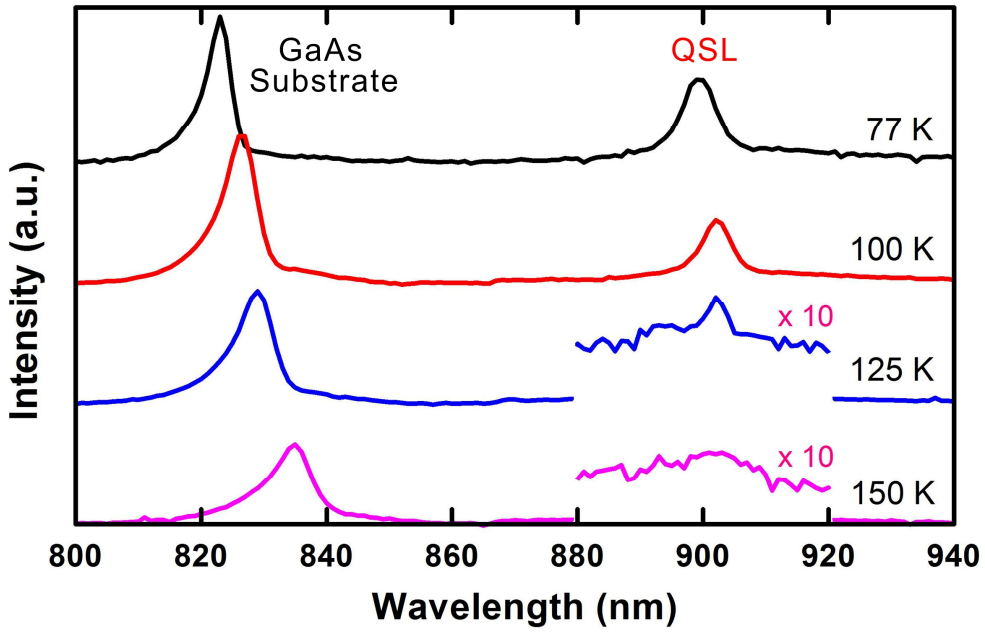

Figure 3.15: PL spectra of a QSL (centered around 900 nm) at 77 K, 100 K, 125 K, and 150 K. The peaks located between 820 nm and 840 nm are from GaAs substrates.

3.4.2 Angular Dependency of Radiation Pattern

Generally, the radiation pattern of optical devices can be altered by means of external microcavity, surface roughening, or photonic crystal [55, 56]. Nonetheless, due to the unique operation principle of QSL, the radiation pattern can also be manipulated

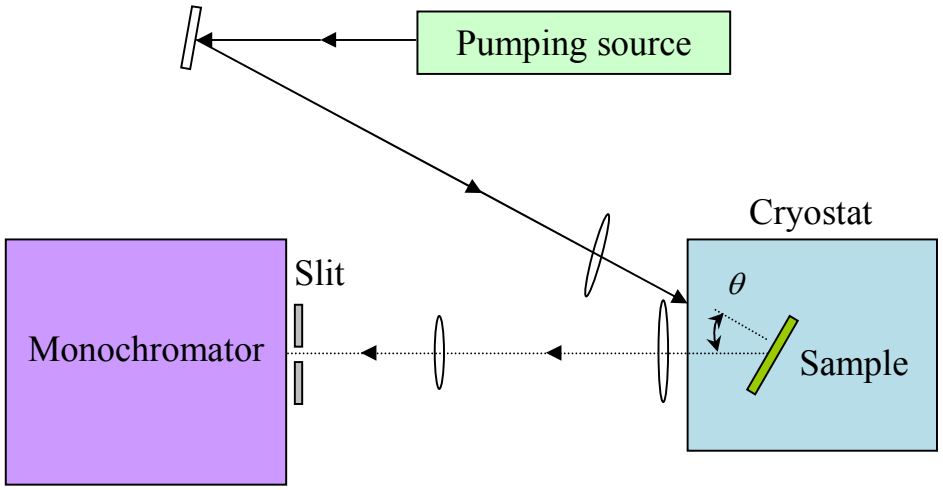

Figure 3.16: Experimental setup for angle-dependent measurement.

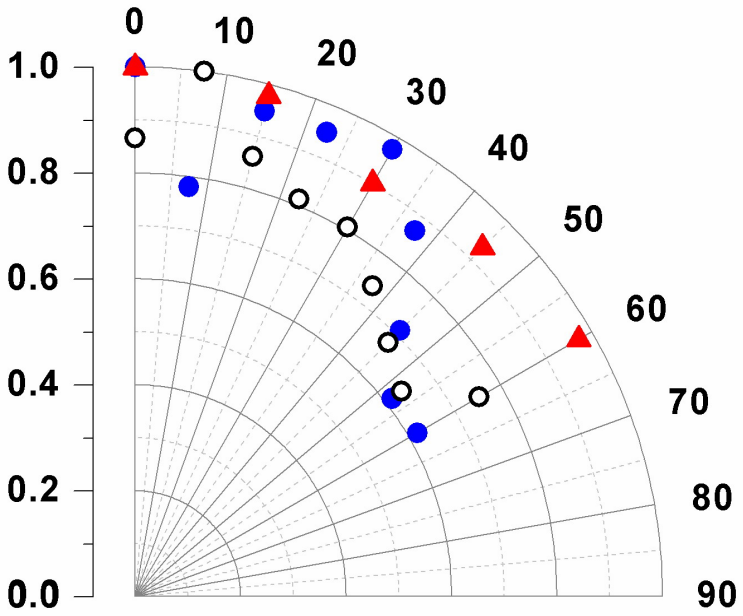

Fig. 3.17: The polar plot of angular dependence of normalized PL peak intensities at 77K in $In_{0.18}Ga_{0.82}As/GaAs$ QSL (solid circle), $In_{0.22}Ga_{0.78}As/GaAs$ QSL (empty circle), and InAs/GaAs SCQDs (solid triangle). Data beyond 60° are not included due to excessive noises.

without the use of any external structures. Since each lattice point in the QSL array acts as an electromagnetic radiation source with the same frequency, the whole QSL array can be viewed as a planar 2-D antenna array. Hence, the radiation beam shape could be controlled by the design of QSL structure.

The angular dependence of a QSL array is measured by rotating the sample inside the cryostat as diagramed in Figure 3.16. The orientation of the sample is defined as 0° when the normal of sample surface lines up with the entrance slit of the spectrometer. A step of 7.5° is used in this measurement. At each angle, the PL intensity of the QSL sample is normalized with respect to that of the unprocessed QW sample. Due to the limit of allowed access angle of the cryostat, the angular dependence measurements are limited to a maximum angle of ~ ±60°. Beyond that, the PL signals are too noisy to be included due to low signal-to-noise ratio.

Figure 3.17 shows the measured angular dependence of PL spectra from two QSL samples and a regrown SCQD sample. For both QSL samples, the PL intensity does not maintain a constant value and drops off quickly at an angle of ~30°. In contrast, the QW sample shows no angular dependency (not shown). Similarly, the radiation pattern of the SCQD sample, which has a wide PL linewidth of ≥100 meV, does not show any angular dependency.

A smaller temperature dependence of the spontaneous emission wavelength exhibited in the QSL structure is attractive for many photonic device applications. Furthermore, shaping of radiation patterns perpendicular to the QSL surface is also important for improving light extraction efficiency in surface emitting photonic devices such as vertical-cavity surface-emitting lasers and light-emitting diodes.

CHAPTER 4 CONCLUSION AND FUTURE WORK

4.1 Summary

In conclusion, two approaches for the fabrication of site-controlled nanostructures are described in this dissertation. By utilizing the soft NIL as the patterning technique, regrown QDs and pillar QDs are fabricated and characterized, and possible applications to QD-based optoelectronics are also explained. Although both methods are promising compared to the traditional serial lithography used in the past, there is still room to improve the performance for either regrown QDs or pillar QDs to be integrated into the devices. More descriptions about process improvement are detailed in the next section.

4.2 Future Work

4.2.1 Regrown QDs

As explained in Section 2.4, large strain is produced during capping of the SCQDs, resulting in a quenched PL at room temperature. Accordingly, scaling down the pattern size will be beneficial to the optical quality of the regrown QDs. Through the discussion of Section 2.3.4, smaller pattern size leads to a wider growth window and stronger PL intensity, and hence is a possible solution to the problem.

A previous attempt used a 100 nm pitch template, which shrank the nanopore size from 100 nm to 50 nm and the pitch from 200 nm to 100 nm, but failed in the end

Figure 4.1 Schematic diagram of PDMS mold fabricated from a (a) 200 nm pitch template, (b) 100 nm pitch template.

due to a pairing problem in the PDMS mold, which arose from the high aspect ratio (the heights of the features divided by their lateral sizes) of the features. As shown in Figure 4.1(b), when the aspect ratio increases, the features tend to collapse and stick together during handling and imprinting process. This leads to numerous defects on the patterned substrate as displayed in Figure 4.2. Even though the array density of patterns is four times higher than that of the original design, a 2:1 aspect ratio makes the 100 nm pitch template almost unusable. As a consequence, the etching depth and the pitch of the feature have to be revised.

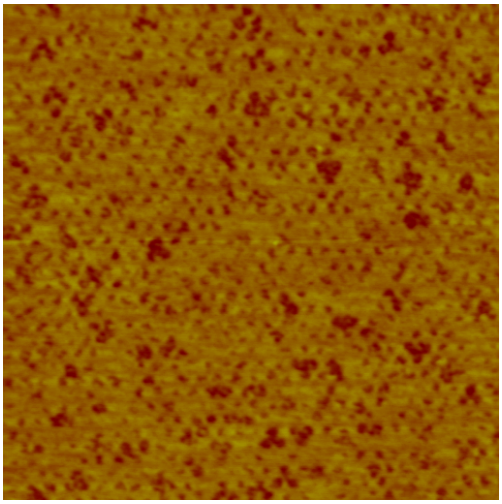

Figure 4.2 AFM image of GaAs substrate after soft NIL with a 100 nm pitch PDMS mold and wet etching. A high density of defects is observed, and the darker region originates from the pairing problem of the PDMS mold.

In the design of a new template, the nanopore diameter remains 50 nm, but the etching depth of the pores is reduced to 65 ± 5 nm. The corresponding aspect ratio is between 1.09 and 1.56, which is a safe regime for successful pattern transfer. However, due to the availability of template, the periodicity is chosen to be 140 nm. The array density will be 5. 1×10^{9} cm^{-2}, and is still two times higher than that of the original design.

After the optical properties of regrown QDs are optimized, regrown QDs will be ready to be integrated into the laser structure for device fabrication. Figure 4.3 shows the layer structure of QD laser. The design is a simple double heterostructure with separate confinement heterojunction for the waveguide layer.

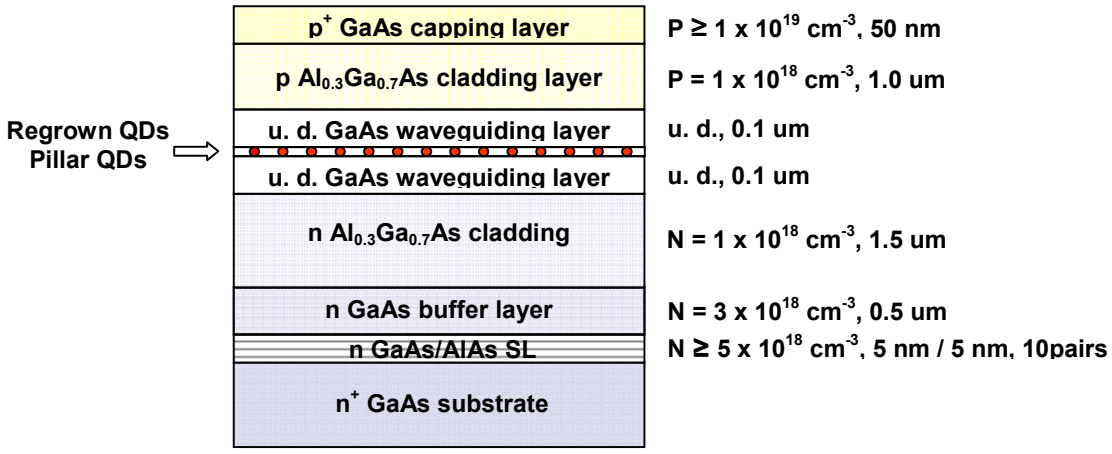

Figure 4.3 Proposed layer structures for QD laser with regrown or pillar QDs integrated in the active region.

For the fabrication of the proposed QD laser, two steps of MBE growth are necessary. To begin with, the bottom half of the laser structure, from buffer layer to the lower GaAs waveguide layer, is grown by SSMBE. Next, the soft NIL and wet etching is

performed on the wafer as described in the previous section. After a sequence of surface treatment, the wafer is loaded into the SSMBE again for the growth of regrown QDs and the top-half structure. Lastly, the sample will be processed into edge-emitting lasers that are characterized, and their performance compared that of reference QW lasers.

The most challenging part of this process is to get decent luminescence after capping the regrown SCQDs. If this problem cannot be solved, making good QD lasers with better performance is almost impossible. Hence, to tackle the problem, switching to the new template with smaller nanopores is the most promising way.

4.2.2 Pillar QDs

In the pillar QDs part, even though the QSL model explains the experimental data reasonably, experimental verification by integrating the QSL structure into optical devices would be more convincing. The proposed structure in Figure 4.3 is suitable for a quick check of this model if simple LED or broad area laser devices are fabricated. Similar to the optimization of the optical properties of regrown QDs, to increase the QD density as well as the luminous efficiency is equally important in the pillar QDs part. Nevertheless, due to the isotropic property of wet etching, the pattern dimension for pillar QD can hardly be scaled down (less than 100 nm) to increase the luminescence intensity. As an alternative, inserting more QWs into each pillar QD might be helpful to improve the optical characteristics of pillar QDs.

Meanwhile, the performance of pillar QDs is still greatly influenced by the process parameters, such as wet etching and surface treatments. The preliminary results of the regrowth of pillar QDs show a reduction of the PL intensities by four times, and

are attributed to nonradiative recombination over the exposed surface. Consequently, the fabrication process must be redesigned to avoid the drawbacks accompanying the wet etching technique. So far, there are two potential substitute methods to fabricate QDs from a QW structure. The first approach is to use diffusion-induced disordering, and the second is to use ion implantation. While maintaining a smooth surface front for the subsequent regrowth step, both approaches are more controllable ways to fabricate pillar QDs by altering the material properties surrounding the pillar QDs.

REFERENCES

[1] N.N. Ledentsov, M. Grundmann, F. Heinrichsdorff, D. Bimberg, V.M. Ustinov, A.E. Zhukov, M.V. Maximov, Z.I. Alferov, and J.A. Lott, "Quantum-dot heterostructure lasers," *IEEE Journal of Selected Topics in Quantum Electronics*, vol. 6, pp. 439-451, 2000.

[2] H. Saito, K. Nishi, I. Ogura, S. Sugou, and Y. Sugimoto, "Room-temperature lasing operation of a quantum-dot vertical-cavity surface-emitting laser," *Applied Physics Letters*, vol. 69, pp. 3140-3142, 1996.

[3] C. Becher, A. Kiraz, P. Michler, W.V. Shoenfeld, P.M. Petroff, L. Zhang, E. Hu, and A. Imamoglu, "A quantum dot single-photon source," *Physica E: Low-dimensional Systems and Nanostructures*, vol. 13, pp. 412-417, Mar. 2002.

[4] M. Asada, Y. Miyamoto, and Y. Suematsu, "Gain and the threshold of three-dimensional quantum-box lasers," *IEEE Journal of Quantum Electronics*, vol. 22, pp. 1915-1921, Sep. 1986.

[5] D. Bimberg, N. Kirstaedter, N. N. Ledentsov, Z. I. Alferov, P. S. Kop'ev, and V. M. Ustinov, "InGaAs-GaAs quantum-dot lasers," *IEEE Journal of Selected Topics in Quantum Electronics*, vol. 3, no. 2, pp. 196-205, Apr. 1997.

[6] D. Bimberg, M. Grundmann, and N. N. Ledentsov, *Quantum Dot Heterostructures*, Wiley, New York, 1998

[7] U. Bimberg, D., Ledentsov, N. N., Grundmann, M., Kirstaedter, N., Schmidt, O. G., Mao, M. H., Ustinov, V. M., Egorov, A. Yu., Kop'ev, P. S., Alferov, Zh. I., Ruvimov, S. S., Gösele and J. Heydenreich, "InAs-GaAs quantum pyramid lasers: *in situ* growth, radiative lifetimes and polarization properties" *Japanese Journal of Applied Physics*, vol. 35, pp. 1311-1319, 1996.

[8] S. J. Xu et al., "Characteristics of InGaAs quantum dot infrared photodetectors," *Applied Physics Letters*, vol. 73, no. 21, p. 3153, 1998.

[9] S. Jeppesen, M.S. Miller, D. Hessman, B. Kowalski, I. Maximov, and L. Samuelson, "Assembling strained InAs islands on patterned GaAs substrates with chemical beam epitaxy," *Applied Physics Letters*, vol. 68, pp. 2228-2230, 1996.

[10] T. Ishikawa, S. Kohmoto, and K. Asakawa, "Site control of self-organized InAs dots on GaAs substrates by in situ electron-beam lithography and molecular-beam epitaxy," *Applied Physics Letters*, vol. 73, pp. 1712-1714, 1998.

[11] S. Kiravittaya, a Rastelli, and O.G. Schmidt, "Photoluminescence from seeded three-dimensional InAs/GaAs quantum-dot crystals," *Applied Physics Letters*, vol. 88, p. 043112, 2006.

[12] Y. Nakamura, O.G. Schmidt, N.Y. Jin-Phillipp, S. Kiravittaya, C. Müller, K. Eberl, H. Gräbeldinger, and H. Schweizer, "Vertical alignment of laterally ordered InAs and InGaAs quantum dot arrays on patterned (001) GaAs substrates," *Journal of Crystal Growth*, vol. 242, pp. 339-344, Jul. 2002.

[13] Y. Morishita, M. Ishiguro, S. Miura, and Y. Enmei, "Molecular-beam epitaxy of InAs on GaAs substrates with hole arrays patterned by focused ion beam," *Journal of Crystal Growth*, vol. 237-239, pp. 1291-1295, Apr. 2002.

[14] J. S. Kim, M. Kawabe, and N. Koguchi, "Ordering of high-quality InAs quantum dots on defect-free nanoholes," *Applied Physics Letters*, vol. 88, p. 072107, 2006.

[15] K. Meneou, K. Y. Cheng, Z. H. Zhang, C. L. Tsai, C. F. Xu, and K. C. Hsieh, "Site-controlled InAs quantum dots regrown on nonlithographically patterned GaAs," *Applied Physics Letters*, vol. 86, no. 15, p. 153114, 2005.

[16] S. Y. Chou, P. R. Krauss, and P. J. Renstrom, "Nanoimprint lithography," *Journal of Vacuum Science & Technology B: Microelectronics and Nanometer Structures*, vol. 14, pp. 4129-4133, 1996.

[17] S. Y. Chou, P. R. Krauss, W. Zhang, L. Guo, and L. Zhuang, "Sub-10 nm imprint lithography and applications," *Journal of Vacuum Science & Technology B: Microelectronics and Nanometer Structures,* vol. 15, pp. 2897-2904, 1997.

[18] K. Meneou and K. Y. Cheng, "Soft photocurable nanoimprint lithography for compound semiconductor nanostructures," *Journal of Vacuum Science & Technology B: Microelectronics and Nanometer Structures*, vol. 26, pp. 156-158, 2008.

[19] H. Schift, "Nanoimprint lithography: An old story in modern times? A review," *Journal of Vacuum Science and Technology B: Microelectronics and Nanometer Structures*, vol. 26, no. 2, pp. 458–480, 2008.

[20] J. Haisma, M. Verheijen, K. van den Heuvel, and J. van den Berg, "Mold-assisted nanolithography: A process for reliable pattern replication," *Journal of Vacuum Science and Technology B: Microelectronics and Nanometer Structures*, vol. 14, no. 6, pp. 4124–4128, 1996.

[21] T.W. Odom, J.C. Love, D.B. Wolfe, K.E. Paul, and G.M. Whitesides, "Improved pattern transfer in soft lithography using composite stamps," *Langmuir*, vol. 18, pp. 5314-5320, 2002.

[22] S. Kiravittaya, H. Heidemeyer, O. G. Schmidt, "Growth of three-dimensional quantum dot crystals on patterned GaAs (001) substrates," *Physica E: Low-dimensional Systems and Nanostructures*, vol. 23, pp. 253-259, Jul. 2004.

[23] E.J. Petit, F. Houzay, and J.M. Moison, "Interaction of atomic hydrogen with native oxides on GaAs (100)," *Journal of Vacuum Science & Technology A: Vacuum, Surfaces, and Films*, vol. 10, pp. 2172-2177, Jul. 1992.

[24] R. Hey, M. Wassermeier, H. M., E. Wiebicke, and H. Kostial, "Minimizing interface contamination in MBE overgrowth," *Journal of Crystal Growth*, vol. 201-202, no. 3, pp. 582-585, May 1999.

[25] J.S. Kim, M. Kawabe, N. Koguchi, D.-Y. Lee, J.S. Kim, and I.-H. Bae, "Structural and optical properties of InAs quantum dots regrown on atomic hydrogen-cleaned GaAs surface," *Applied Physics Letters*, vol. 87, 261914, 2005.

[26] H.-C. Kan, S. Shah, T. Tadyyon-Eslami, and R.J. Phaneuf, "Transient evolution of surface roughness on patterned GaAs (001) during homoepitaxial growth," *Physical Review Letters*, vol. 92, 146101, 2004.

[27] G. Biasiol and E. Kapon, "Mechanisms of self-ordering of quantum nanostructures grown on nonplanar surfaces," *Physical Review Letters*, vol. 81, pp. 2962-2965, Oct. 1998.

[28] L. Chu, M. Arzberger, G. Böhm, and G. Abstreiter, "Influence of growth conditions on the photoluminescence of self-assembled InAs/GaAs quantum dots," *Journal of Applied Physics*, vol. 85, pp. 2355-2362, 1999.

[29] T. Chung, G. Walter, and N. Holonyak, Jr., "Growth mechanism of InAs quantum dots on GaAs by metal-organic chemical-vapor deposition," *Journal of Applied Physics*, vol. 97, p. 053510, 2005.

[30] C.-C. Cheng, K. Meneou, and K.Y. Cheng, "High optical quality InAs site-controlled quantum dots grown on soft photocurable nanoimprint lithography patterned GaAs substrates," *Applied Physics Letters*, vol. 95, p. 173108, 2009.

[31] P. Atkinson, S.P. Bremner, D. Anderson, G.A.C. Jones, and D.A. Ritchie, "Size evolution of site-controlled InAs quantum dots grown by molecular beam epitaxy on prepatterned GaAs substrates," *Journal of Vacuum Science & Technology B: Microelectronics and Nanometer Structures*, vol. 24, pp. 1523-1526, 2006.

[32] D. Feketa, K.T. Chan, J.M. Ballantyne, and L.F. Eastman, "Graded-index separate-confinement InGaAs/GaAs strained-layer quantum well laser grown by metalorganic chemical vapor deposition," *Applied Physics Letters*, vol. 49, pp. 1659-1660, 1986.

[33] Y.J. Yang, K.Y. Hsieh, and R.M. Kolbas, "Continuous room-temperature operation of an InGaAs-GaAs-AlGaAs strained-layer laser," *Applied Physics Letters*, vol. 51, pp. 215-217, 1987.

[34] K. J. Meneou, "Pathways for quantum dot optoelectronics fabrication using soft nanoimprint lithography," Ph.D. dissertation, University of Illinois at Urbana-Champaign, 2010.

[35] E. W. Berg and S. W. Pang, "Electrical and optical characteristics of etch induced damage in InGaAs," *Journal of Vacuum Science & Technology B: Microelectronics and Nanometer Structures*, vol. 16, no. 6, p. 3359, Nov. 1998.

[36] R. Steffen, T. Koch, J. Oshinowo, F. Faller, and A. Forchel, "Photoluminescence study of deep etched InGaAs/GaAs quantum wires and dots defined by low-voltage electron beam lithography," *Applied Physics Letters*, vol. 68, pp. 223-225, 1996.

[37] X. Qian, J. Li, D. Wasserman, and W.D. Goodhue, "Uniform InGaAs quantum dot arrays fabricated using nanosphere lithography," *Applied Physics Letters*, vol. 93, p. 231907, 2008.

[38] R. Steffen, J. Oshinowo, T. Koch, and A. Forchel, "InGaAs/GaAs quantum wires and dots defined by low-voltage electron-beam lithography," *Journal of Vacuum Science & Technology B: Microelectronics and Nanometer Structures*, vol. 13, pp. 2888-2891, Nov. 1995.

[39] Z.Y. AbuWaar, E. Marega Jr, M. Mortazavi, and G.J. Salamo, "In situ photoluminescence study of uncapped InAs/GaAs quantum dots," *Nanotechnology*, vol. 19, p. 335712, Aug. 2008.

[40] D.R. Scifres, R.D. Burnham, and W. Streifer, "Distributed-feedback single heterojunction GaAs diode laser," *Applied Physics Letters*, vol. 25, pp. 203-206, Sep. 1974.

[41] E. M. Purcell, "Spontaneous emission probabilities at radio frequencies," *Physical Review*, vol. 69, pp. 681, 1946.

[42] E. Yablonovich, "Inhibited spontaneous emission in solid-state physics and electronics," *Physical Review Letters,* vol. 58, pp. 2059-2062, 1987.

[43] S. John, "Strong localization of photons in certain disordered dielectric superlattices," *Physical Review Letters,* vol. 58, pp. 2486-2489, 1987.

[44] G. Björk, S. Machida, Y. Tamamoto, and K. Igeta, "Modification of spontaneous emission rate in planar dielectric microcavity structures," *Physical Review A,* vol. 44, pp. 669-681, 1991.

[45] H. Yokoyama, K. Nishi, T. Anan, H. Yamada, S. D. Brorson, and E. P. Ippen, "Enhanced spontaneous emission from GaAs quantum wells in monolithic microcavities," *Applied Physics Letters,* vol. 57, pp. 2814-2816, 1990.

[46] H. Kogelnik and C. V. Shank, "Stimulated emission in a periodic structure," *Applied Physics Letters,* vol. 18, pp. 152-154, 1971.

[47] S. D. Brorson, H. Yokoyama, and E. P. Ippen, "Spontaneous emission rate alteration in optical waveguide structures," *IEEE Journal of Selected Topics in Quantum Electronics,* vol. 26, pp. 1492-1499, 1990.

[48] A. Y. Cho, "GaAs epitaxy by a molecular beam method: observations of surface structure on the (001) face," *Journal of Applied Physics,* vol. 42, pp. 2074-2081, 1971.

[49] J. S. Blakemore, "Semiconducting and other major properties of gallium arsenide," *Journal of Applied Physics*, vol. 53, p. R123-R181, 1982.

[50] P. Parayanthal and F. H. Pollak, "Raman scattering in alloy semiconductors: "spatial correlation" model," *Physical Review Letters,* vol. 52, pp. 1822-1825, 1984.

[51] M. Nakamura, K. Aiki, J. Umeda, A. Yariv, H. W. Yen, and T. Morikawa, "GaAs-$Ga_{1-x}Al_xAs$ double-heterostructure distributed-feedback diode lasers," *Applied Physics Letters,* vol. 25, pp. 487-488, 1974.

[52] T. Takamori, a. R. Pratt, and T. Kamijoh, "Temperature dependence of InGaAs/GaAs quantum well microcavity light-emitting diodes," *Applied Physics Letters*, vol. 74, no. 24, p. 3598, 1999.

[53] D. E. Wohlert, S. T. Chou, a. C. Chen, K. Y. Cheng, and K. C. Hsieh, "Observation of temperature-insensitive emission wavelength in GaInAs strained multiple-quantum-wire heterostructures," *Applied Physics Letters*, vol. 68, no. 17, p. 2386, 1996.

[54] K. Mukai and M. Sugawara, "Suppression of temperature sensitivity of interband emission energy in 1.3-μm-region by an InGaAs overgrowth on self-assembled InGaAs/GaAs quantum dots," *Applied Physics Letters*, vol. 74, no. 26, p. 3963, 1999.

[55] C. Dill, R. P. Stanley, U. Oesterle, D. Ochoa, and M. Ilegems, "Effect of detuning on the angular emission pattern of high-efficiency microcavity light-emitting diodes," *Applied Physics Letters*, vol. 73, no. 26, p. 3812, 1998.

[56] J. J. Wierer, M. R. Krames, J. E. Epler, N. F. Gardner, M. G. Craford, J. R.Wendt, J. A. Simmons, and M. M. Sigalas, "InGaN/GaN quantum-well heterostructure light-emitting diodes employing photonic crystal structures," *Applied Physics Letters*, vol. 84, no. 19, p. 3885, 2004.